A mathematical model that integrates cardiac electrophysiology, mechanics and fluid dynamics: application to the human left heart

Bucelli, M.; Zingaro, A.; Africa, P. C.; Fumagalli, I.; Dede', L.;

Quarteroni, A.

MOX, Dipartimento di Matematica
Politecnico di Milano, Via Bonardi 9 - 20133 Milano (Italy)

mox-dmat@polimi.it   http://mox.polimi.it

A mathematical model that integrates cardiac electrophysiology, mechanics and fluid dynamics: application to the human left heart

Michele Bucelli[1,*], Alberto Zingaro[1], Pasquale Claudio Africa[1],
Ivan Fumagalli[1], Luca Dede'[1], Alfio Quarteroni[1,2]

[1] MOX, Department of Mathematics, Politecnico di Milano, P.zza Leonardo da Vinci 32, 20133 Milan, Italy
[2] Mathematics Institute, EPFL, Av. Piccard, CH-1015 Lausanne, Switzerland (Professor Emeritus)

August 10, 2022

Abstract

We propose a mathematical and numerical model for the simulation of the heart function that couples cardiac electrophysiology, active and passive mechanics and hemodynamics, and includes reduced models for cardiac valves and the circulatory system. Our model accounts for the major feedback effects among the different processes that characterize the heart function, including electro-mechanical and mechano-electrical feedback as well as force-strain and force-velocity relationships. Moreover, it provides a three-dimensional representation of both the cardiac muscle and the hemodynamics, coupled in a fluid-structure interaction (FSI) model. By leveraging the multiphysics nature of the problem, we discretize it in time with a segregated electrophysiology-force generation-FSI approach, allowing for efficiency and flexibility in the numerical solution. We employ a monolithic approach for the numerical discretization of the FSI problem. We use finite elements for the spatial discretization of those partial differential equations that contribute to the model. We carry out a numerical simulation on a realistic human left heart model, obtaining results that are qualitatively and quantitatively in agreement with physiological ranges and medical images.

Keywords: multiphysics modeling, cardiac modeling, electromechanics, fluid-structure interaction, blood circulation

1   Introduction

Cardiovascular diseases represent the major cause of death in the adult population of the western world [16]. While in-vivo measuring techniques allow to inspect and quantify the heart function and dysfunction, these measures often lack resolution or accuracy, and may be invasive. Mathematical models for computational medicine can provide tools to simulate the human heart function, complementing experimental measurements, providing further insight into the cardiac function, and assisting in the development of personalized treatments [54, 60, 77, 96, 110, 109].

The heart function results from the interplay of several different physical processes [79, 81], ranging from the sub-cellular scale to the tissue one. Electrochemical processes drive the excitation of cardiac muscular cells, resulting in the generation of an active force during contraction that, together with the passive mechanical properties of the cardiac tissue, interacts with the blood within the heart chambers, pumping it towards the circulatory system. Understanding and then modeling the multiphysics and multiscale nature of the heart function, as well as feedback effects among its components, is crucial for constructing an accurate computational model of the heart [69, 99, 110, 125].

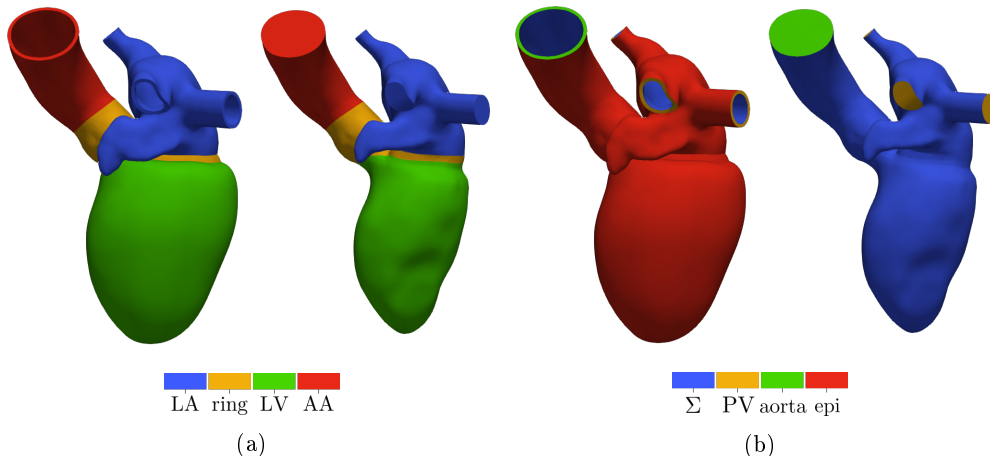* Corresponding author, email address: `michele.bucelli@polimi.it`

Figure 1: Solid (left) and fluid (right) computational domains. Colors represent the partition into Ω_i^{LV}, Ω_i^{LA}, Ω_i^{AA} and Ω_i^{ring} in (a), with $i \in \{s, f\}$, and the different boundary portions in (b).

Several mathematical and numerical heart models have been proposed in recent years. Most of them focus on some specific feature of the heart function, by surrogating the remaining ones with models of reduced dimensionality: electrophysiology [5, 24, 36, 58, 106, 118, 140, 143], cardiac mechanics and electromechanics [9, 10, 35, 46, 54, 56, 63, 86, 105, 107, 115, 123, 132, 141] or computational fluid dynamics (CFD) of the blood [26, 30, 77, 83, 116, 129, 137, 139, 142, 155, 156]. Only few works also consider the interplay between hemodynamics and cardiac mechanics in a fluid-structure interaction (FSI) framework [25, 41, 49, 53, 66], while neglecting or simplifying the electrical processes generating the contraction [21, 80, 97, 153].

Albeit each of the above mentioned models can provide meaningful insight into the cardiac function in both healthy and pathological conditions, they often neglect the feedback mechanisms that relate the different components. On the other hand, fully integrated models featuring multiphysics coupling of electrophysiology, mechanics and fluid dynamics [23, 55, 125, 134, 145] can provide a very accurate description of the physics of the heart, at the price of a high model complexity and large computational cost.

One of the first fully coupled heart models was provided by the UT-Heart simulator [69, 99, 134], and was subsequently employed for personalized clinical case studies [78]. Another fully coupled model was proposed in [125]. There, the authors focus on right and left ventricular systole, while providing a simplified description of the atria and neglecting the presence of valves. In [147, 148], a coupled fluid-structure-electrophysiology left heart model is presented, relying on the immersed boundary method in a finite elements/finite differences combined framework for the numerical discretization. The model uses a simplified phenomenological description of force generation [95], neglecting feedbacks from fiber shortening; moreover, the interplay between heart and circulation is treated in a simplified approach. The same authors also provide a GPU-accelerated version of the same model in [149] for computational speedup. Finally, in [11], a simplified 2D fluid-structure-electrophysiology interaction model is developed for embryonic hearts. To the best of our knowledge, no other works focus on a fully integrated model of the heart.

In this work, we propose a novel multiphysics coupled model featuring a three-dimensional description of cardiac electrophysiology, active and passive mechanics, and hemodynamics, together with a closed-loop lumped-parameter model to simulate systemic and pulmonary circulation. We will refer to the different physical components (electrophysiology, contractile force generation, mechanics, fluid dynamics, circulation) as *core models*. The proposed model includes several of the feedback mechanisms that regulate the heart function, including mechano-electric feedbacks [124], force-strain and force-velocity relationships [113], FSI between the blood and the muscle [22], and the feedback between the heart and the circulation [67, 115, 156]. In particular, the feedback between force generation and fiber shortening and shortening velocity was found to be highly important in cardiac electromechanics [46]. Moreover, FSI modeling allows to capture dynamic

2

effects such as the presence of pressure gradients and pressure waves, overcoming some of the limitations of uncoupled CFD and electromechanics models [139, 154]. We test our model on a realistic human left heart, comprising the left ventricle, left atrium and a portion of the ascending aorta, as well as the mitral and aortic valves.

Due to the complexity and large scale of the problem at hand, it is crucial to employ efficient numerical schemes for its solution. A critical issue is the numerical treatment of the coupling conditions between the different core models. One possible approach is to solve the fully coupled problem monolithically [55]. However, this requires the development of complex solvers and ad-hoc preconditioners, and it lacks flexibility in the choice of the discretization schemes and parameters for each core model. Inspired by [115], we choose a segregated-staggered scheme, in which all coupling terms are treated explicitly when possible. Implicit, monolithic coupling is used for fluid-structure interaction [22]. Spatial discretization is achieved by means of the finite element method [71, 108]. The proposed computational framework leverages high-performance computing techniques to enable large-scale simulations, based on the finite element library $\texttt{life}^{\texttt{x}}$ [1, 2, 87].

We run a numerical simulation and compare the value of several indicators against normal ranges, obtaining a satisfactory agreement. A qualitative match with physiological behavior is also observed in terms of ventricular pressure and volume traces, as well as three dimensional deformation and flow patterns. Overall, the results indicate that the proposed computational framework can provide an accurate and physiologically sound description of the physics of the heart.

This paper is structured as follows: in Section 2, we present in detail the mathematical models employed. Section 3 describes the numerical scheme, and Section 4 presents and analyzes the simulation results. Finally, in Section 5, we point at some shortcomings in the proposed model, and, in Section 6, we draw some conclusive remarks.

2 Mathematical models

Let $\Omega \subset \mathbb{R}^3$ be an open, bounded domain, changing in time and representing the volume occupied by a human left heart at every time instant during the heartbeat. We partition the domain into the subdomains Ω_f and Ω_s (see Figure 1), representing the volume occupied by the blood and that occupied by the solid heart wall respectively. We denote their interface by $\Sigma = \partial\Omega_\text{f} \cap \partial\Omega_\text{s}$. We further partition the fluid and solid subdomains into $\Omega_\text{i}^\text{LV}$, $\Omega_\text{i}^\text{LA}$, $\Omega_\text{i}^\text{AA}$ and $\Omega_\text{i}^\text{ring}$, for i $\in \{\text{f},\text{s}\}$, representing the left ventricle (LV), the left atrium (LA), the ascending aorta (AA) and the atrioventricular ring, for either the fluid or the solid domains. On the boundary of any of the defined sets, $\mathbf{n}$ denotes the outward directed normal unit vector. On Σ, $\mathbf{n}$ denotes the normal unit vector directed outward from the fluid domain and inward into the solid domain.

All the previously defined domains are moving in time as the heart beats (to keep the notation light, we omit the explicit dependence of the domains on time). We define a fixed *reference configuration* $\widehat{\Omega}$ to keep track of the deformation. For each of the previously defined sets, we use a hat to denote the corresponding set in reference configuration. We refer to the moving configuration as the *current configuration*. The evolution in time of the current configuration is described by the following maps:

$$\mathcal{L}_\text{s} : \widehat{\Omega}_\text{s} \times (0,T) \to \Omega_\text{s} \qquad \Omega_\text{s} = \{\mathbf{x} = \mathcal{L}_\text{s}(\widehat{\mathbf{x}},t)\,, \widehat{\mathbf{x}} \in \widehat{\Omega}_\text{s}\}\,,$$
$$\mathcal{L}_\text{f} : \widehat{\Omega}_\text{f} \times (0,T) \to \Omega_\text{f} \qquad \Omega_\text{f} = \{\mathbf{x} = \mathcal{L}_\text{f}(\widehat{\mathbf{x}},t)\,, \widehat{\mathbf{x}} \in \widehat{\Omega}_\text{f}\}\,.$$

The precise definition of the maps depends on the physical models defined on each subdomain, and is detailed in the following sections.

We denote by $t \in (0,T)$ the independent variable representing time, by $\mathbf{x}$ the spatial coordinates in the current configuration, and by $\widehat{\mathbf{x}}$ the spatial coordinates in reference configuration.

We consider a coupled problem involving several physical models: electrophysiology, active force generation, cardiac FSI and circulation hemodynamics. The unknowns of the model are determined by solving a coupled system of differential equations representing an *electrophysiology-mechanics-fluid dynamics* (EMF)

interaction problem:

$$v : \widehat{\Omega}_{\mathrm{s}}^{\mathrm{LV}} \times (0, T) \to \mathbb{R} \qquad\qquad \text{transmembrane potential,}$$

$$\mathbf{w} : \widehat{\Omega}_{\mathrm{s}}^{\mathrm{LV}} \times (0, T) \to \mathbb{R}^{N_{\mathrm{ion}}^{\mathbf{w}}} \qquad\qquad \text{ionic gating variables,}$$

$$\mathbf{z} : \widehat{\Omega}_{\mathrm{s}}^{\mathrm{LV}} \times (0, T) \to \mathbb{R}^{N_{\mathrm{ion}}^{\mathbf{z}}} \qquad\qquad \text{ionic concentrations,}$$

$$\mathbf{s} : \widehat{\Omega}_{\mathrm{s}}^{\mathrm{LV}} \times (0, T) \to \mathbb{R}^{N_{\mathrm{act}}} \qquad\qquad \text{activation state,}$$

$$\mathbf{d} : \widehat{\Omega}_{\mathrm{s}} \times (0, T) \to \mathbb{R}^{3} \qquad\qquad \text{solid displacement,}$$

$$\mathbf{d}_{\mathrm{ALE}} : \widehat{\Omega}_{\mathrm{f}} \times (0, T) \to \mathbb{R}^{3} \qquad\qquad \text{fluid domain displacement,}$$

$$\mathbf{u} : \Omega_{\mathrm{f}} \times (0, T) \to \mathbb{R}^{3} \qquad\qquad \text{fluid velocity,}$$

$$p : \Omega_{\mathrm{f}} \times (0, T) \to \mathbb{R} \qquad\qquad \text{pressure,}$$

$$\mathbf{c} : (0, T) \to \mathbb{R}^{N_{\mathrm{circ}}} \qquad\qquad \text{circulation state variables.}$$

The remainder of this section is devoted to the description of the models and equations that compose the EMF problem. In the following, we omit the numerical values of all the parameters mentioned, that can be found in Appendix D.

2.1 Fiber generation

Cardiac tissue is organized in sheets of fibers, which determine a preferential direction for the conduction of the electrical signal [79, 81, 117], and are relevant in characterizing the passive and active mechanical properties of the cardiac muscle [43, 57]. We incorporate fibers in the model by defining, at every point $\widehat{\mathbf{x}} \in \widehat{\Omega}_{\mathrm{s}}$, a local orthonormal basis $\{\mathbf{f}_0, \mathbf{s}_0, \mathbf{n}_0\}$ representing the local direction of fibers, fiber sheets and normal to fiber sheets [106].

As the fiber direction is rarely available from experimental data, it is often reconstructed in a preprocessing step using rule-based algorithms [39, 106, 119]. For our left heart model, we combine different Laplace-Dirichlet Rule-Based Methods (LDRBMs), namely the one presented in [12] for ventricular fibers and the one presented in [106] for left atrial fibers.

2.2 Electrophysiology

Cardiac cells can be excited by an electrical stimulus, triggering a series of subcellular mechanisms resulting in an *action potential* that manifests as a variation in time of the *transmembrane potential* [29, 79, 81, 135], i.e. the difference of potential between the intracellular and extracellular spaces.

We model the ventricle $\widehat{\Omega}_{\mathrm{s}}^{\mathrm{LV}}$ as electrically excitable, while other portions of the solid domain, including $\widehat{\Omega}_{\mathrm{s}}^{\mathrm{LA}}$, are regarded as electrically passive, i.e. they do not generate action potentials. We remark that this is a simplification for what concerns the LA (see Section 5).

The evolution of the transmembrane potential v is described by the monodomain equation [29] augmented with the mechano-electric feedbacks [124]. Let $F = I + \nabla \mathbf{d}$ and $J = \det F$. The monodomain equation reads

$$\begin{cases} J\chi C_{\mathrm{m}} \dfrac{\partial v}{\partial t} - \nabla \cdot \left(J F^{-1} D_{\mathrm{m}} F^{-T} \nabla v \right) + J\chi I_{\mathrm{ion}}(v, \mathbf{w}, \mathbf{z}) = J\chi I_{\mathrm{app}}(\widehat{\mathbf{x}}, t) & \text{in } \widehat{\Omega}_{\mathrm{s}}^{\mathrm{LV}} \times (0, T) \,, \\ J F^{-1} D_{\mathrm{m}} F^{-T} \nabla v \cdot \mathbf{n} = 0 & \text{on } \partial\widehat{\Omega}_{\mathrm{s}}^{\mathrm{LV}} \times (0, T) \,, \\ v = v_0 & \text{in } \widehat{\Omega}_{\mathrm{s}}^{\mathrm{LV}} \times \{0\} \,, \end{cases} \qquad (1)$$

where χ and C_{m} are the membrane surface-to-volume ratio and membrane capacitance, respectively.

The vector $\mathbf{w}$ collects the recovery (or gating) variables [29], that for a single cell represent fractions of open ionic channels, while $\mathbf{z}$ is a vector of ionic concentrations. Most notably, one of the variables within the vector $\mathbf{z}$ represents the intracellular calcium concentration $[\mathrm{Ca}^{2+}]_{\mathrm{i}}$. The evolution of $\mathbf{w}$ and $\mathbf{z}$ is modeled by

coupling (1) with the ionic model by Ten Tusscher and Panfilov [136], which also defines the ionic current $I_{\mathrm{ion}}(v, \mathbf{w}, \mathbf{z})$. The model is expressed by a system of ODEs defined at each point $\widehat{\mathbf{x}} \in \widehat{\Omega}_{\mathrm{s}}^{\mathrm{LV}}$:

$$
\begin{cases}
\dfrac{\partial \mathbf{w}}{\partial t} = \mathbf{F}_{\mathrm{ion}}^{\mathbf{w}}(v, \mathbf{w}) & \text{in } \widehat{\Omega}_{\mathrm{s}}^{\mathrm{LV}} \times (0, T) , \\[2mm]
\dfrac{\partial \mathbf{z}}{\partial t} = \mathbf{F}_{\mathrm{ion}}^{\mathbf{z}}(v, \mathbf{w}, \mathbf{z}) & \text{in } \widehat{\Omega}_{\mathrm{s}}^{\mathrm{LV}} \times (0, T) , \\[2mm]
\mathbf{w} = \mathbf{w}_0 & \text{in } \widehat{\Omega}_{\mathrm{s}}^{\mathrm{LV}} \times \{0\} , \\[2mm]
\mathbf{z} = \mathbf{z}_0 & \text{in } \widehat{\Omega}_{\mathrm{s}}^{\mathrm{LV}} \times \{0\} .
\end{cases}
$$

We remark that $\mathbf{F}_{\mathrm{ion}}^{\mathbf{w}}$ and $\mathbf{F}_{\mathrm{ion}}^{\mathbf{z}}$ do not involve spatial derivatives of $\mathbf{w}$, $\mathbf{z}$ or v. For the precise definition of $\mathbf{F}_{\mathrm{ion}}^{\mathbf{w}}$, $\mathbf{F}_{\mathrm{ion}}^{\mathbf{z}}$ and I_{ion}, we refer to [136]. The initial states v_0, $\mathbf{w}_0$ and $\mathbf{z}_0$ are obtained by solving a reduced, zero-dimensional monodomain equation for a large number of heartbeats, until a periodic limit cycle is reached [29, 115].

The tensor D_{m} in (1) incorporates the conductivity properties of the tissue, and is defined as

$$
D_{\mathrm{m}} = \sigma_{\mathrm{m}}^{\mathrm{l}} \frac{F\mathbf{f}_0 \otimes F\mathbf{f}_0}{\|F\mathbf{f}_0\|^2} + \sigma_{\mathrm{m}}^{\mathrm{t}} \frac{F\mathbf{s}_0 \otimes F\mathbf{s}_0}{\|F\mathbf{s}_0\|^2} + \sigma_{\mathrm{m}}^{\mathrm{n}} \frac{F\mathbf{n}_0 \otimes F\mathbf{n}_0}{\|F\mathbf{n}_0\|^2} . \tag{2}
$$

Here, $\sigma_{\mathrm{m}}^{\mathrm{l}}$, $\sigma_{\mathrm{m}}^{\mathrm{t}}$ and $\sigma_{\mathrm{m}}^{\mathrm{n}}$ are conductivities in the direction of sheets, fibers and normal to sheets respectively.

The formulations of both the monodomain equation (1) and the conductivity tensor (2) incorporate the so-called geometry-mediated mechano-electric feedback mechanisms, through the terms J and F [28, 123, 124, 140] that account for the fact that the electrical stimulus is propagating in a deforming medium.

Finally, I_{app} is a time-dependent forcing term that provides the initial stimulus. We impose an applied current on three points $\widehat{\mathbf{x}}_{\mathrm{app}}^0$, $\widehat{\mathbf{x}}_{\mathrm{app}}^1$ and $\widehat{\mathbf{x}}_{\mathrm{app}}^2$ on the endocardial surface of the ventricle, to trigger the electrical activation (Figure 2a). The applied current has the following analytical expression:

$$
I_{\mathrm{app}}(\widehat{\mathbf{x}}, t) = \begin{cases}
\displaystyle\sum_{i=0}^{3} A_{\mathrm{app}} \exp\left\{ -\left(\frac{\|\widehat{\mathbf{x}} - \widehat{\mathbf{x}}_{\mathrm{app}}^i\|}{\sigma_{\mathrm{app}}} \right)^2 \right\} & \text{if } t \in (0, T_{\mathrm{app}}] , \\[4mm]
0 & \text{if } t > T_{\mathrm{app}} .
\end{cases}
$$

This mimics the effect of the Purkinje network [32, 36, 85, 118, 143], which is not included in our model. The stimulus is repeated every $T_{\mathrm{hb}} = 800\,\mathrm{ms}$ to obtain multiple heartbeats.

2.3 Force generation model

In response to the electrical excitation, muscular cells shorten, generating an active contractile force. As done for the electrophysiology, we model the ventricle $\widehat{\Omega}_{\mathrm{s}}^{\mathrm{LV}}$ as actively contracting, whereas all other subdomains are treated as mechanically passive.

We use the activation model RDQ20-MF presented in [113]. The model is biophysically detailed, in the sense that it provides an explicit representation of the subcellular mechanisms leading to the generation of contractile force. Moreover, it includes the feedback between force generation and sarcomere length, responsible for the Frank-Starling mechanism [73, 79, 81, 100], and between force generation and fiber shortening velocity [17, 79]. Both were found to be fundamental in capturing accurately the heart function, especially for what concerns the hemodynamics [46].

The RDQ20-MF model is expressed in terms of a system of ODEs defined at each point of $\widehat{\Omega}_{\mathrm{s}}^{\mathrm{LV}}$:

$$
\begin{cases}
\dfrac{\partial \mathbf{s}}{\partial t} = \mathbf{F}_{\mathrm{act}}\left(\mathbf{s}, [\mathrm{Ca}^{2+}]_i, SL, \dfrac{\partial SL}{\partial t} \right) & \text{in } \widehat{\Omega}_{\mathrm{s}}^{\mathrm{LV}} \times (0, T) , \\[3mm]
\mathbf{s} = \mathbf{s}_0 & \text{in } \widehat{\Omega}_{\mathrm{s}}^{\mathrm{LV}} \times \{0\} .
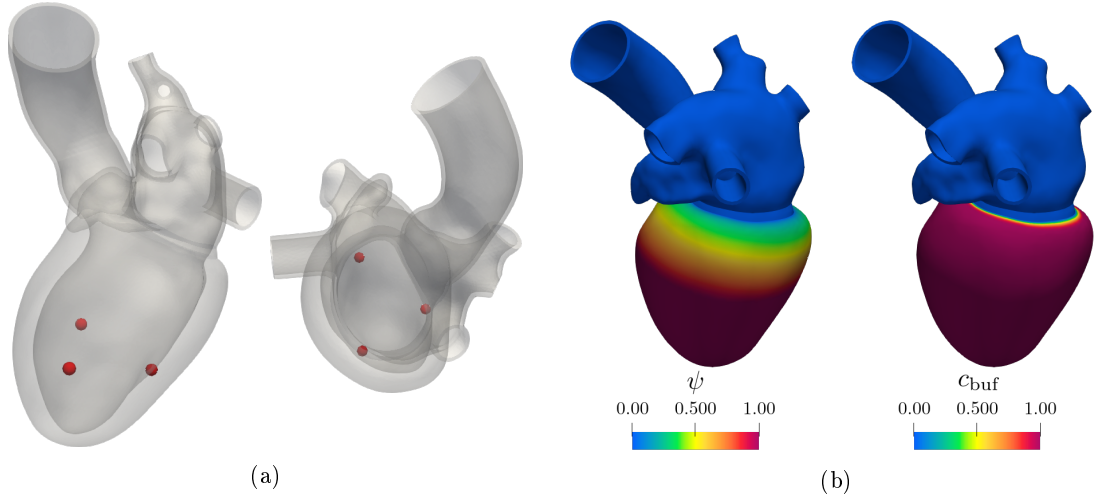\end{cases} \tag{3}
$$

Figure 2: (a) Stimulation points (red) on the left ventricular endocardium. (b) Functions ψ (left) and c_{buf} used in the regularization of the interface between ventricle and atrioventricular ring.

In the above system, $\mathbf{s}$ is a vector of variables defining the contraction state of cardiac cells, and SL is the sarcomere length, defined as $SL = SL_0\sqrt{I_{4\mathrm{f}}}$. SL_0 is the sarcomere length at rest [113] and $I_{4\mathrm{f}} = F\mathbf{f}_0 \cdot F\mathbf{f}_0$ is a measure of the stretch along the fibers.

In practice, to compute SL, we solve the following regularization problem:

$$\begin{cases} -\delta_{SL}^2 \Delta SL + SL = SL_0\sqrt{I_{4\mathrm{f}}} & \text{in } \widehat{\Omega}_\mathrm{s} \times (0,T) \,, \\ \delta_{SL}^2 \nabla SL \cdot \mathbf{n} = 0 & \text{on } \partial\widehat{\Omega}_\mathrm{s} \times (0,T) \,, \end{cases} \tag{4}$$

with δ_{SL} a suitable regularization radius parameter. This has the effect of preventing sharp variations of SL over spatial scales smaller than δ_{SL} [115].

The generated active force is computed at every point $\widehat{\mathbf{x}} \in \widehat{\Omega}_\mathrm{s}^{\mathrm{LV}}$ as a function $T_{\mathrm{act}}(\mathbf{s})$ of the contraction state $\mathbf{s}$. For the precise definition of $\mathbf{F}_{\mathrm{act}}$ and T_{act}, we refer to [113]. The force-velocity relationship may yield instabilities, which are prevented with a numerically consistent stabilization as described in [114].

The initial state $\mathbf{s}_0$ is obtained by solving the system (3) uncoupled from the other models, until a steady state solution is reached.

2.4 Solid mechanics

The deformation of the heart wall is modeled in a Lagrangian reference framework with the elastodynamics equation [98]. The vector $\mathbf{d}$ describes the displacement of the solid domain, so that

$$\mathcal{L}_\mathrm{s}(\widehat{\mathbf{x}}, t) = \widehat{\mathbf{x}} + \mathbf{d}(\widehat{\mathbf{x}}, t) \qquad \widehat{\mathbf{x}} \in \widehat{\Omega}_\mathrm{s} \,, t \in (0,T) \,.$$

Let $\widehat{\Gamma}_\mathrm{s}^{\mathrm{epi}} \subset \partial\widehat{\Omega}_\mathrm{s}\backslash\widehat{\Sigma}$ be the epicardial boundary, corresponding to the outer wall of the heart, $\widehat{\Gamma}_\mathrm{s}^{\mathrm{PV}} \subset \partial\widehat{\Omega}_\mathrm{s}\backslash\widehat{\Sigma}$ be the portion of the boundary corresponding to the pulmonary veins sections, and $\widehat{\Gamma}_\mathrm{s}^{\mathrm{ao}} \subset \partial\widehat{\Omega}_\mathrm{s}\backslash\widehat{\Sigma}$ be the one

corresponding to the AA terminal section (Figure 1b). The equations for solid mechanics read

$$
\begin{cases}
\rho_{\mathrm{s}} \dfrac{\partial^2 \mathbf{d}}{\partial t^2} - \nabla \cdot P_{\mathrm{s}}(\mathbf{d}, \mathbf{s}) = \mathbf{0} & \text{in } \widehat{\Omega}_{\mathrm{s}} \times (0, T) , \\[2mm]
\mathbf{d} = \mathbf{0} & \text{on } \left(\widehat{\Gamma}_{\mathrm{s}}^{\mathrm{PV}} \cup \widehat{\Gamma}_{\mathrm{s}}^{\mathrm{ao}} \right) \times (0, T) , \\[2mm]
P_{\mathrm{s}}(\mathbf{d}, \mathbf{s}) \mathbf{n} = -(\mathbf{n} \otimes \mathbf{n}) \left(K_{\perp}^{\mathrm{epi}} \mathbf{d} + C_{\perp}^{\mathrm{epi}} \dfrac{\partial \mathbf{d}}{\partial t} \right) & \\
\qquad\quad - (I - \mathbf{n} \otimes \mathbf{n}) \left(K_{\parallel}^{\mathrm{epi}} \mathbf{d} + C_{\parallel}^{\mathrm{epi}} \dfrac{\partial \mathbf{d}}{\partial t} \right) & \text{on } \widehat{\Gamma}_{\mathrm{s}}^{\mathrm{epi}} \times (0, T) , \\[2mm]
\mathbf{d} = \mathbf{d}_0 & \text{in } \widehat{\Omega}_{\mathrm{s}} \times \{0\} .
\end{cases}
\tag{5}
$$

In the above system, ρ_{s} is the density of the solid and $P_{\mathrm{s}}(\mathbf{d}, \mathbf{s})$ is the first Piola-Kirchhoff stress tensor. The stress tensor incorporates both the passive and the active mechanical properties of the material. We work in the active stress framework [4, 59, 63, 102, 109, 115, 126], decomposing the stress tensor into the sum of a passive and an active term:

$$
P_{\mathrm{s}}(\mathbf{d}, \mathbf{s}) = P_{\mathrm{pas}}(\mathbf{d}) + P_{\mathrm{act}}(\mathbf{d}, \mathbf{s}) .
$$

The passive part is obtained as the derivative of a strain energy function $\mathcal{W}$ that characterizes the mechanical properties of the material [98]:

$$
P_{\mathrm{pas}}(\mathbf{d}) = \frac{\partial \mathcal{W}}{\partial F} .
$$

We use the Guccione anisotropic constitutive law [61, 141] in $\widehat{\Omega}_{\mathrm{s}}^{\mathrm{LV}}$ and in $\widehat{\Omega}_{\mathrm{s}}^{\mathrm{LA}}$. In $\widehat{\Omega}_{\mathrm{s}}^{\mathrm{AA}}$ and $\widehat{\Omega}_{\mathrm{s}}^{\mathrm{ring}}$ we use an isotropic neo-Hookean material model [98]. In both cases, we treat the solid as nearly incompressible, by penalizing local volume variations in the strain energy function. See Appendix A for the definitions of the constitutive laws.

The active part of the stress tensor is computed as a function of the activation state, through

$$
P_{\mathrm{act}}(\mathbf{d}, \mathbf{s}) = T_{\mathrm{act}}(\mathbf{s}) \frac{F \mathbf{f}_0 \otimes \mathbf{f}_0}{\sqrt{I_{4\mathrm{f}}}} .
$$

The boundary conditions imposed on the mechanics equations are a homogeneous Dirichlet condition on $\widehat{\Gamma}_{\mathrm{s}}^{\mathrm{PV}}$ and $\widehat{\Gamma}_{\mathrm{s}}^{\mathrm{ao}}$ [54], and a generalized visco-elastic Robin boundary condition on $\widehat{\Gamma}_{\mathrm{s}}^{\mathrm{epi}}$. The latter has the purpose of modeling the presence of the pericardial sac, that surrounds the heart and provides mechanical support [105, 132]. Finally, no boundary conditions are prescribed on $\widehat{\Sigma}$ since the interface conditions for the fluid-solid coupling are set on that portion of $\partial \widehat{\Omega}_{\mathrm{s}}$ (see Section 2.7).

2.4.1 Initial conditions

We start from a model of the left heart that corresponds to a configuration reconstructed from CT and MRI scans [157]. Such configuration is subject to the load of blood pressure on the endocardial wall, while the elastodynamics equations (5) are formulated assuming that $\widehat{\Omega}_{\mathrm{s}}$ is stress-free. Therefore, as a preprocessing step, we compute a stress-free reference configuration using the unloading algorithm presented in [115].

From there, we determine the initial condition for the solid displacement $\mathbf{d}_0$ by solving a quasi-static ramp, as described in [115], imposing an initial pressure p_0 on the endocardial wall. We choose p_0 to match typical values at the end of the diastolic phase. We remark that different initial pressures p_0^{LA}, p_0^{ring}, p_0^{LV} and p_0^{AA} are prescribed on the boundaries of the different chambers [46].

2.4.2 Material interface regularization

The different material models used result in sharp discontinuities across the interface between the atrioventricular ring subdomain and the atrium and ventricle subdomains. These do not constitute an issue from the point of view of solid mechanics. However, they lead to the formation of corners at the fluid-solid interface, which pose a relevant numerical issue for the fluid domain displacement inducing mesh elements distortion (see Section 2.5). To overcome it, we regularize the interface between $\widehat{\Omega}_{\mathrm{s}}^{\mathrm{LV}}$ and $\widehat{\Omega}_{\mathrm{s}}^{\mathrm{ring}}$ as follows. As a pre-processing step, a Laplace problem is solved to obtain a function ψ that varies smoothly from 0 in $\widehat{\Omega}_{\mathrm{s}}^{\mathrm{ring}}$ to 1 in the apical portion of $\widehat{\Omega}_{\mathrm{s}}^{\mathrm{LV}}$. We then set

$$c_{\mathrm{buf}}(\widehat{\mathbf{x}}) = \frac{1}{2}\left[1 - \cos\left(\frac{\pi \min\{\psi, \psi_{\mathrm{th}}\}}{\psi_{\mathrm{th}}}\right)\right] \, ,$$

where ψ_{th} is a threshold value that controls the size of the regularization region. Both ψ and c_{buf} are depicted in Figure 2b. Finally, we redefine the stress tensor in $\widehat{\Omega}_{\mathrm{s}}^{\mathrm{LV}}$ as a convex combination of the Guccione (G) and neo-Hookean (NH) stress tensors so that the transition between the material of the ventricle (or the atrium) and the atrioventricular ring is smooth:

$$P_{\mathrm{pas}}(\mathbf{d}) = c_{\mathrm{buf}}\, P_{\mathrm{G}}(\mathbf{d}) + (1 - c_{\mathrm{buf}})\, P_{\mathrm{NH}}(\mathbf{d}) \, .$$

The regularization is included at the interfaces between $\widehat{\Omega}_{\mathrm{s}}^{\mathrm{LV}}$ and $\widehat{\Omega}_{\mathrm{s}}^{\mathrm{ring}}$ and between $\widehat{\Omega}_{\mathrm{s}}^{\mathrm{LA}}$ and $\widehat{\Omega}_{\mathrm{s}}^{\mathrm{ring}}$.

2.5 Fluid domain displacement

We account for the motion of Ω_{f} in the arbitrary Lagrangian-Eulerian (ALE) framework [38, 72, 131]. The vector $\mathbf{d}_{\mathrm{ALE}}$ represents the displacement of the fluid domain, such that

$$\mathcal{L}_{\mathrm{f}}(\widehat{\mathbf{x}}, t) = \widehat{\mathbf{x}} + \mathbf{d}_{\mathrm{ALE}}(\widehat{\mathbf{x}}, t) \qquad \widehat{\mathbf{x}} \in \widehat{\Omega}_{\mathrm{f}} \, , t \in (0, T) \, .$$

Inspired by [68, 127], we use a fictitious non-linear solid material to model the displacement of the fluid domain, so that $\mathbf{d}_{\mathrm{ALE}}$ solves at every time t the following stationary problem:

$$\begin{cases} -\nabla \cdot P_{\mathrm{ALE}}(\mathbf{d}_{\mathrm{ALE}}) = \mathbf{0} & \text{in } \widehat{\Omega}_{\mathrm{f}} \, , \\ \mathbf{d}_{\mathrm{ALE}} = \mathbf{d} & \text{on } \widehat{\Sigma} \, , \\ \mathbf{d}_{\mathrm{ALE}} = \mathbf{0} & \text{on } \widehat{\Gamma}_{\mathrm{f}}^{\mathrm{PV}} \cup \widehat{\Gamma}_{\mathrm{f}}^{\mathrm{ao}} \, , \end{cases} \tag{6}$$

wherein

$$P_{\mathrm{ALE}} = \frac{1}{q}\left(I - \left(F_{\mathrm{ALE}}F_{\mathrm{ALE}}^{T}\right)^{-1}\right) \, ,$$
$$F_{\mathrm{ALE}} = I + \nabla \mathbf{d}_{\mathrm{ALE}} \, .$$

In the above, q is a scale-invariant mesh quality metric that has the purpose of stiffening the regions of the fluid domain with highly distorted element, aiming at preventing solver breakdown. It is defined element-wise as

$$q(\widehat{\mathbf{x}}) = \frac{|D_{\mathrm{ALE}}|_{\mathrm{F}}^{2}}{3(\det D_{\mathrm{ALE}})^{\frac{2}{3}}} \, ,$$

where $D_{\mathrm{ALE}} = F_{\mathrm{ALE}} \nabla \mathcal{M}$ and $\mathcal{M}$ is the linear mapping from the unit simplex to the element in current configuration.

We remark that (6) is non-linear, since P_{ALE} is a non-linear function of $\mathbf{d}_{\mathrm{ALE}}$. Therefore, its solution is significantly more complex and costly than that of other typically used operators, such as the harmonic extension operator [22, 153, 156] or linear elasticity [76, 131]. On the other hand, however, we found that this results in an increased robustness with respect to large deformations, preventing the inversion of mesh elements, that would result in the breakdown of the numerical solver.

8

We define the ALE velocity as the time derivative of $\mathbf{d}_{\mathrm{ALE}}$, pushed forward to the current configuration, namely

$$\mathbf{u}_{\mathrm{ALE}}(\mathbf{x},t) = \frac{\partial \mathbf{d}_{\mathrm{ALE}}}{\partial t} \left(\mathcal{L}_{\mathrm{f}}^{-1}(\mathbf{x},t), t \right) \ .$$

2.6 Fluid dynamics

The evolution of fluid velocity $\mathbf{u}$ and pressure p is prescribed by the Navier-Stokes equations for a Newtonian, incompressible fluid [108]:

$$\begin{cases} \rho_{\mathrm{f}} \left[\dfrac{\partial \mathbf{u}}{\partial t} + ((\mathbf{u} - \mathbf{u}_{\mathrm{ALE}}) \cdot \nabla) \mathbf{u} \right] - \nabla \cdot \sigma_{\mathrm{f}}(\mathbf{u}, p) + \mathcal{R}(\mathbf{u}, \mathbf{u}_{\mathrm{ALE}}) = \mathbf{0} & \text{in } \Omega_{\mathrm{f}} \times (0, T), & \text{(7a)} \\[2mm] \nabla \cdot \mathbf{u} = 0 & \text{in } \Omega_{\mathrm{f}} \times (0, T), & \text{(7b)} \\[2mm] \sigma_{\mathrm{f}}(\mathbf{u}, p)\mathbf{n} = -p_{\mathrm{in}}(t)\mathbf{n} & \text{on } \Gamma_{\mathrm{f}}^{\mathrm{PV}} \times (0, T), & \text{(7c)} \\[2mm] \sigma_{\mathrm{f}}(\mathbf{u}, p)\mathbf{n} = -p_{\mathrm{out}}(t)\mathbf{n} & \text{on } \Gamma_{\mathrm{f}}^{\mathrm{ao}} \times (0, T), & \text{(7d)} \\[2mm] \mathbf{u} = \mathbf{0} & \text{in } \Omega_{\mathrm{f}} \times \{0\}. & \text{(7e)} \end{cases}$$

In the above system, ρ_{f} denotes the fluid density, and the stress tensor σ_{f} is given by

$$\sigma_{\mathrm{f}}(\mathbf{u}, p) = \mu_{\mathrm{f}} \left(\nabla \mathbf{u} + \nabla \mathbf{u}^T \right) - pI \ ,$$

where μ_{f} is the dynamic viscosity. $\mathcal{R}(\mathbf{u})$ is a resistive term that accounts for the presence of valves in a penalty-based approach (see Section 2.6.1) [31, 45, 51, 52, 50, 156].

In analogy with the solid mechanics problem (Section 2.4), no boundary conditions are prescribed on Σ since, on that portion of $\partial \Omega_{\mathrm{f}}$, the interface conditions for the fluid-solid coupling are imposed (see Section 2.7). The functions $p_{\mathrm{in}}(t)$ and $p_{\mathrm{out}}(t)$ are pressures provided by the circulation model (see Section 2.8) for the pulmonary venous and systemic arterial circulation compartments, respectively.

2.6.1 Valve modeling

Heart compartments are separated by valves that prevent reverse flow [79]. For a left heart model, the mitral valve (MV) separates the LV and the LA, and the aortic valve (AV) separates the LV and the AA. Accurate modeling and numerical simulation of the valves is challenging: the valves are thin structures, they undergo large displacements, and contact phenomena play a major role in their physiological function [8, 33, 41, 66, 70, 89, 128, 138]. Our interest mainly lies in the macroscopic effect of the opening and closing of the valves onto the blood flow, rather than on an accurate description of valves motion. In particular, we want our model to describe the role of valves in ensuring the correct direction of the flow through the heart, and to capture the formation of jets and vortices associated to the presence of valve leaflets.

Therefore, we use a reduced approach for the modeling of valves, based on the Resistive Immersed Implicit Surface (RIIS) method [45, 51, 52, 156, 154]. Each valve, at any time $t \in (0, T)$, is represented by a surface Γ_{k}^t, $\mathrm{k} \in \{\mathrm{MV}, \mathrm{AV}\}$, immersed in the fluid domain. For $\mathrm{k} \in \{\mathrm{MV}, \mathrm{AV}\}$, let $\varphi_{\mathrm{k}}^t(\mathbf{x})$ be the signed distance function from the surface Γ_{k}^t. The Navier-Stokes momentum equation (7a) includes the penalization term $\mathcal{R}(\mathbf{u}, \mathbf{u}_{\mathrm{ALE}})$ forcing the fluid velocity to match the valve velocity (with respect to the moving frame of the domain) near the immersed surfaces:

$$\mathcal{R}(\mathbf{u}, \mathbf{u}_{\mathrm{ALE}}) = \sum_{\mathrm{k} \in \{\mathrm{MV}, \mathrm{AV}\}} \frac{R_{\mathrm{k}}}{\varepsilon_{\mathrm{k}}} \delta_{\varepsilon_{\mathrm{k}}}(\varphi_{\mathrm{k}}^t(\mathbf{x}))(\mathbf{u} - \mathbf{u}_{\mathrm{ALE}} - \mathbf{u}_{\Gamma_{\mathrm{k}}}) \ .$$

In the above, R_{k} are resistance parameters, ε_{k} are valves half-thicknesses, $\mathbf{u}_{\Gamma_{\mathrm{k}}}$ is the valve velocity with respect to the moving domain, and $\delta_{\varepsilon_{\mathrm{k}}}$ is a smoothed delta function, defined as

$$\delta_{\varepsilon_{\mathrm{k}}}(y) = \begin{cases} \dfrac{1}{2\varepsilon_{\mathrm{k}}} \left(1 + \cos\left(\dfrac{\pi y}{\varepsilon_{\mathrm{k}}} \right) \right) & \text{if } |y| \leq \varepsilon_{\mathrm{k}} \ , \\[3mm] 0 & \text{if } |y| > \varepsilon_{\mathrm{k}} \ . \end{cases}$$

We account for the opening and closing of valves by deforming the corresponding surfaces. Although we do not include any FSI model for the valves, their opening and closing times are determined based on the pressure jump across the immersed surfaces while the durations of opening and closing are prescribed. We refer to [156] and Appendix B for more details.

2.6.2 Flow stabilization and turbulence modeling

Blood flow in the heart chambers is characterized by a regime of transition to turbulence [20, 144, 146, 155, 156]. To account for that, we use the VMS-LES model for fine scales [13, 155]. We refer the interested reader to [13] for details on the VMS-LES approach to turbulence modeling.

We set Neumann boundary conditions on boundaries $\Gamma_{\mathrm{f}}^{\mathrm{PV}}$ and $\Gamma_{\mathrm{f}}^{\mathrm{ao}}$. Neumann conditions may cause instability phenomena in case of inflow [18, 93]. Therefore, we make use of backflow stabilization in the form of inertial stabilization as presented in [18]: Neumann boundary conditions are modified by imposing

$$\begin{cases} \sigma_{\mathrm{f}}(\mathbf{u}, p)\mathbf{n} = -p_{\mathrm{in}}(t)\mathbf{n} + \beta \dfrac{\rho_{\mathrm{f}}}{2}|\mathbf{u} \cdot \mathbf{n}|_{-}\mathbf{u} & \text{on } \Gamma_{\mathrm{f}}^{\mathrm{PV}} \times (0, T) \,, \\ \sigma_{\mathrm{f}}(\mathbf{u}, p)\mathbf{n} = -p_{\mathrm{out}}(t)\mathbf{n} + \beta \dfrac{\rho_{\mathrm{f}}}{2}|\mathbf{u} \cdot \mathbf{n}|_{-}\mathbf{u} & \text{on } \Gamma_{\mathrm{f}}^{\mathrm{ao}} \times (0, T) \,, \end{cases}$$

where $|\mathbf{u} \cdot \mathbf{n}|_{-} = \min\{\mathbf{u} \cdot \mathbf{n}, 0\}$ and $\beta = 1$.

2.7 Fluid-structure interaction

The fluid and solid models are coupled by kinematic and dynamic interface conditions on Σ that prescribe the continuity of velocity and of stresses [14, 22]:

$$\begin{cases} \mathbf{u} = \dfrac{\partial \mathbf{d}}{\partial t} & \text{on } \Sigma \times (0, T) \,, \\ \sigma_{\mathrm{f}}(\mathbf{u}, p)\mathbf{n} = \sigma_{\mathrm{s}}(\mathbf{d}, \mathbf{s})\mathbf{n} & \text{on } \Sigma \times (0, T) \,. \end{cases}$$

In the above, $\sigma_{\mathrm{s}}(\mathbf{d})$ is the Cauchy stress tensor for the solid, related to the first Piola-Kirchhoff tensor by

$$J\sigma_{\mathrm{s}}(\mathbf{d}, \mathbf{s}) = F P_{\mathrm{s}}(\mathbf{d}, \mathbf{s})^T \,.$$

2.8 Circulation model

Inlet and outlet conditions for the fluid model are provided by a zero-dimensional circulation model [19, 67, 115, 156], representing the whole closed-loop circulation with a lumped-parameter approach. It includes four different circulation compartments (systemic arterial, systemic venous, pulmonary arterial and pulmonary venous) as well as the four heart chambers. Using an electric circuit analogy [67] represented in Figure 3, the circulation compartments are modeled as RLC circuits, heart chambers are modeled as time-varying elastances, and valves are modeled as non-ideal diodes.

In order to couple it to the three-dimensional FSI model, we remove from the full circulation model those compartments that have a three-dimensional description, that is the left atrium, the left ventricle, and mitral and aortic valves [156]. The remaining unknowns are the volumes and pressures of the right atrium and ventricle (V_{RA}, p_{RA}, V_{RV} and p_{RV}), pressures and flow rates through the four circulation compartments, except for the pulmonary venous flow rate ($p_{\mathrm{AR}}^{\mathrm{SYS}}$, $Q_{\mathrm{AR}}^{\mathrm{SYS}}$, $p_{\mathrm{VEN}}^{\mathrm{SYS}}$, $Q_{\mathrm{VEN}}^{\mathrm{SYS}}$, $p_{\mathrm{AR}}^{\mathrm{PUL}}$, $Q_{\mathrm{AR}}^{\mathrm{PUL}}$ and $p_{\mathrm{VEN}}^{\mathrm{PUL}}$), and flow rates through tricuspid and pulmonary valves (Q_{PV} and Q_{TV}). Collecting all the circulation variables into the vector $\mathbf{c}(t)$, the circulation problem can be stated in compact form as a differential-algebraic equation:

$$\mathbf{F}_{\mathrm{circ}}\left(\frac{\partial \mathbf{c}}{\partial t}, \mathbf{c}, t\right) = \mathbf{0} \,.$$

Refer to Appendix C for the definition of $\mathbf{F}_{\mathrm{circ}}$.

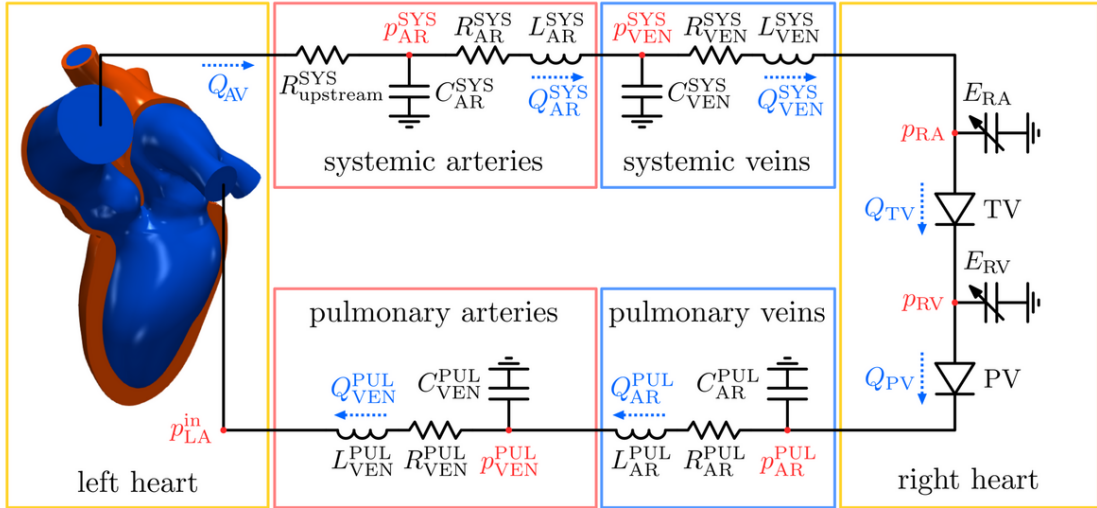Figure 3: Circuital (0D) representation for the circulation model coupled to the EMF model. Refer to Appendix C for the model equations.

Following [111, 156], the 0D circulation model is coupled to the 3D fluid model by imposing the continuity of stresses and of fluxes at the 3D-0D interface: for $t \in (0, T)$,

$$p_{\text{in}}(t) = p_{\text{LA}}^{\text{in}}(t) \ ,$$

$$p_{\text{out}}(t) = p_{\text{AR}}^{\text{SYS}}(t) + R_{\text{upstream}}^{\text{SYS}} Q_{\text{AV}}(t) \ ,$$

$$Q_{\text{VEN}}^{\text{PUL}}(t) = -\int_{\Gamma_{\text{f}}^{\text{PV}}} (\mathbf{u} - \mathbf{u}_{\text{ALE}}) \cdot \mathbf{n} d\gamma \ ,$$

$$Q_{\text{AV}}(t) = \int_{\Gamma_{\text{f}}^{\text{ao}}} (\mathbf{u} - \mathbf{u}_{\text{ALE}}) \cdot \mathbf{n} d\gamma \ .$$

We remark that, with respect to [156], we include the resistance term $R_{\text{upstream}}^{\text{SYS}} Q_{\text{AV}}(t)$ when coupling the outlet to the systemic arterial compartment. This has the role of avoiding reflections of pressure waves at the outlet, that would otherwise result in unphysical oscillations [74]. $p_{\text{LA}}^{\text{in}}(t)$ is the pressure downstream of the pulmonary veins compartment (Figure 3).

3 Numerical discretization

We detail the discretization strategy used to numerically solve the fully coupled EMF problem, starting from the semi-discretization in time (Section 3.1) and then describing spatial discretization (Section 3.2).

3.1 Time discretization

We introduce a partition of the time interval $(0, T)$ into sub-intervals $(t_i, t_{i+1}]$, with $i = 0, 1, \ldots, N_T$, $t_0 = 0$ and $t_{N_T} = T$, and such that $t_{i+1} - t_i = \Delta t$ for all i. From here on, we denote the approximation of any of the solution variables at a given timestep t_n with the superscript n, e.g. $\mathbf{u}^n \approx \mathbf{u}(t_n)$.

We employ a staggered scheme for the coupling of the different systems of equations, schematically represented in Figure 4. The scheme is based on solving separately the different subproblems, using an explicit coupling whenever stability is not a concern. We remark that we use an implicit coupling of the FSI problem [22]. The scheme is derived from that in [115] for the electromechanics of the left ventricle, adapted to include the three dimensional description of the blood hemodynamics.
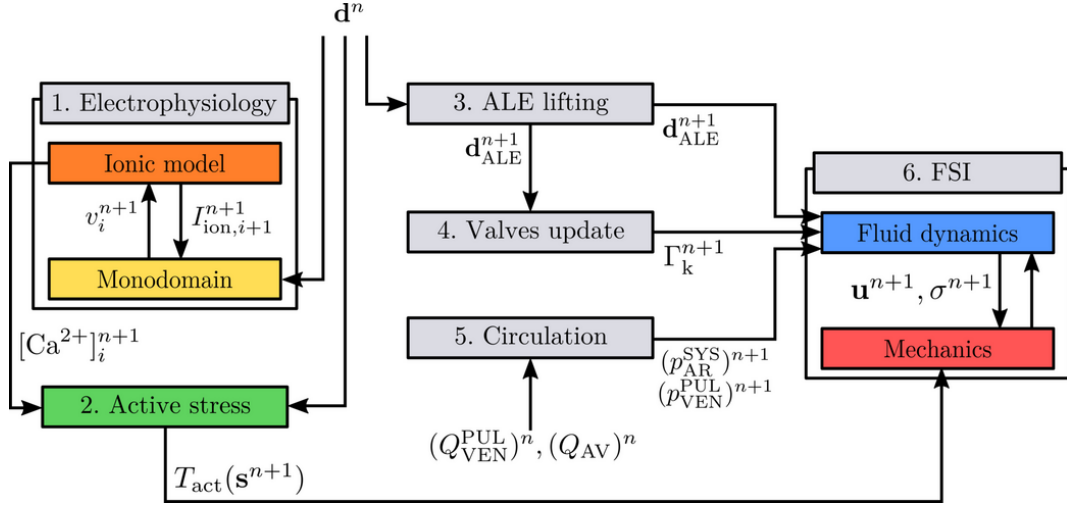
11

Figure 4: Time advancing scheme for the coupled model. The numbers correspond to the steps described in Section 3.1.

We use finite differences for the approximation of time derivatives appearing in the different model equations. Electrophysiology is characterized by a faster dynamics than the other models, and requires a smaller timestep for an accurate solution [115]. Therefore, we discretize it with a timestep $\Delta t_{\mathrm{EP}} = \dfrac{\Delta t}{N_{\mathrm{EP}}}$, with $N_{\mathrm{EP}} \in \mathbb{N}$. Given the solution variables and the domain Ω_{f}^n at timestep t_n, in order to compute the solution at timestep t_{n+1} we perform the following steps:

1. Electrophysiology: we solve N_{EP} time advancing steps of the electrophysiology problem, that is: setting $v_0^{n+1} = v^n$ and $\mathbf{w}_0^{n+1} = \mathbf{w}^n$, for $i = 0, 1, \ldots, N_{\mathrm{EP}} - 1$:

   (a) we compute $\mathbf{w}_{i+1}^{n+1}$ and $\mathbf{z}_{i+1}^{n+1}$ by solving the ionic model

$$\begin{cases} \dfrac{\mathbf{w}_{i+1}^{n+1} - \mathbf{w}_i^{n+1}}{\Delta t_{\mathrm{EP}}} = \mathbf{F}_{\mathrm{ion}}^{\mathbf{w}}(v_i^{n+1}, \mathbf{w}_{i+1}^{n+1}) & \text{in } \widehat{\Omega}_{\mathrm{s}}^{\mathrm{LV}} \,, \\[2ex] \dfrac{\mathbf{z}_{i+1}^{n+1} - \mathbf{z}_i^{n+1}}{\Delta t_{\mathrm{EP}}} = \mathbf{F}_{\mathrm{ion}}^{\mathbf{z}}(v_i^{n+1}, \mathbf{w}_i^{n+1}, \mathbf{z}_i^{n+1}) & \text{in } \widehat{\Omega}_{\mathrm{s}}^{\mathrm{LV}} \,. \end{cases} \tag{8}$$

   We use an implicit-explicit (IMEX) scheme, with an implicit discretization of gating variables and an explicit discretization of ionic concentrations [112, 115].

   (b) Then, we solve the monodomain equation to compute v_{i+1}^{n+1}:

$$\begin{cases} J^n \chi C_{\mathrm{m}} \dfrac{v_{i+1}^{n+1} - v_i^{n+1}}{\Delta t_{\mathrm{EP}}} - \nabla \cdot \left(J^n (F^n)^{-1} D_{\mathrm{m}} (F^n)^{-T} \nabla v_{i+1}^{n+1} \right) & \text{in } \widehat{\Omega}_{\mathrm{s}}^{\mathrm{LV}} \,, \\[1ex] \quad + J^n \chi I_{\mathrm{ion}}(v_i^{n+1}, \mathbf{w}_{i+1}^{n+1}, \mathbf{z}_{i+1}^{n+1}) = J^n \chi I_{\mathrm{app}}(\widehat{\mathbf{x}}, t^n + (i+1)\Delta t_{\mathrm{EP}}) & \\[2ex] J^n (F^n)^{-1} D_{\mathrm{m}} (F^n)^{-T} \nabla v_{i+1}^{n+1} \cdot \mathbf{n} = 0 & \text{on } \partial\widehat{\Omega}_{\mathrm{s}}^{\mathrm{LV}} \,. \end{cases} \tag{9}$$

   System (9) relies on a semi-implicit discretization, since the ionic current term is computed using the trasmembrane potential at previous subiteration, v_i^{n+1}. Therefore, the problem is linear.

   We set $v^{n+1} = v_{N_{\mathrm{EP}}}^{n+1}$, $\mathbf{w}^{n+1} = \mathbf{w}_{N_{\mathrm{EP}}}^{n+1}$ and $\mathbf{z}^{n+1} = \mathbf{z}_{N_{\mathrm{EP}}}^{n+1}$;

2. Force generation model: we compute SL^n solving (4) using $\mathbf{d}^n$ to compute $I_{4\mathrm{f}}$, then we solve the activation model to compute $\mathbf{s}^{n+1}$:

$$\frac{\mathbf{s}^{n+1} - \mathbf{s}^n}{\Delta t} = \mathbf{F}_{\mathrm{act}}\left(s^n, [\mathrm{Ca}^{2+}]_i^{n+1}, SL^n, \frac{SL^n - SL^{n-1}}{\Delta t} \right) ; \tag{10}$$

3. Fluid domain displacement: we compute $\mathbf{d}_{\mathrm{ALE}}^{n+1}$ by solving

$$\begin{cases} -\nabla \cdot P_{\mathrm{ALE}}(\mathbf{d}_{\mathrm{ALE}}^{n+1}) = \mathbf{0} & \text{in } \widehat{\Omega}_{\mathrm{f}} , \\ \mathbf{d}_{\mathrm{ALE}}^{n+1} = \mathbf{d}^n & \text{on } \widehat{\Sigma} , \\ \mathbf{d}_{\mathrm{ALE}}^{n+1} = \mathbf{0} & \text{on } \widehat{\Gamma}_{\mathrm{f}}^{\mathrm{PV}} \cup \widehat{\Gamma}_{\mathrm{f}}^{\mathrm{ao}} . \end{cases} \tag{11}$$

We remark that we compute $\mathbf{d}_{\mathrm{ALE}}^{n+1}$ from the displacement $\mathbf{d}^n$ from the previous timestep, so that the geometric FSI coupling condition is treated explicitly. We then update the fluid domain $\Omega_{\mathrm{f}}^{n+1}$ according to the displacement $\mathbf{d}_{\mathrm{ALE}}^{n+1}$ and compute

$$\mathbf{u}_{\mathrm{ALE}}^{n+1}(\mathbf{x}) = \frac{\mathbf{d}_{\mathrm{ALE}}^{n+1}\left(\left(\mathcal{L}_{\mathrm{f}}^{n+1}\right)^{-1}(\mathbf{x}) \right) - \mathbf{d}_{\mathrm{ALE}}^n\left(\left(\mathcal{L}_{\mathrm{f}}^n\right)^{-1}(\mathbf{x}) \right)}{\Delta t} ;$$

4. Valves position: we update the position of the valves according to their opening state and to $\mathbf{d}_{\mathrm{ALE}}^{n+1}$, computing the surfaces $\Gamma_{\mathrm{MV}}^{n+1}$ and $\Gamma_{\mathrm{AV}}^{n+1}$ (see Appendix B);

5. Circulation: we compute the flow rates at the 3D-0D interface as

$$(Q_{\mathrm{VEN}}^{\mathrm{PUL}})^{n+1} = -\int_{\Gamma_{\mathrm{f}}^{\mathrm{PV}}} (\mathbf{u}^n - \mathbf{u}_{\mathrm{ALE}}^{n+1}) \cdot \mathbf{n} d\gamma ,$$

$$Q_{\mathrm{AV}}^{n+1} = \int_{\Gamma_{\mathrm{f}}^{\mathrm{ao}}} (\mathbf{u}^n - \mathbf{u}_{\mathrm{ALE}}^{n+1}) \cdot \mathbf{n} d\gamma ,$$

then advance the circulation model (2.8) with an explicit Runge-Kutta scheme [108], to compute $\mathbf{c}^{n+1}$;

6. Fluid-structure interaction: we solve the FSI problem to compute $\mathbf{d}^{n+1}, \mathbf{u}^{n+1}, p^{n+1}$:

$$\begin{cases} \rho_{\mathrm{f}} \dfrac{\mathbf{d}^{n+1} - 2\mathbf{d}^n + \mathbf{d}^{n-1}}{\Delta t^2} - \nabla \cdot P_{\mathrm{s}}(\mathbf{d}^{n+1}, \mathbf{s}^{n+1}) = \mathbf{0} & \text{in } \widehat{\Omega}_{\mathrm{s}} , \\[2mm] \mathbf{d}^{n+1} = \mathbf{0} & \text{on } \widehat{\Gamma}_{\mathrm{s}}^{\mathrm{PV}} \cup \widehat{\Gamma}_{\mathrm{s}}^{\mathrm{ao}} , \\[2mm] \begin{aligned} P_{\mathrm{s}}(\mathbf{d}^{n+1}, \mathbf{s}^{n+1})\mathbf{n} = & -(\mathbf{n} \otimes \mathbf{n})\left(K_{\perp}^{\mathrm{epi}}\mathbf{d}^{n+1} + C_{\perp}^{\mathrm{epi}} \dfrac{\mathbf{d}^{n+1} - \mathbf{d}^n}{\Delta t} \right) \\ & -(I - \mathbf{n} \otimes \mathbf{n})\left(K_{\parallel}^{\mathrm{epi}}\mathbf{d}^{n+1} + C_{\parallel}^{\mathrm{epi}} \dfrac{\mathbf{d}^{n+1} - \mathbf{d}^n}{\Delta t} \right) \end{aligned} & \text{on } \widehat{\Gamma}_{\mathrm{s}}^{\mathrm{epi}} , \\[4mm] \begin{aligned} \rho_{\mathrm{f}} & \left[\dfrac{\mathbf{u}^{n+1} - \mathbf{u}^n}{\Delta t} + ((\mathbf{u}^{n+1} - \mathbf{u}_{\mathrm{ALE}}^{n+1}) \cdot \nabla)\mathbf{u}^{n+1} \right] \\ & -\nabla \cdot \sigma_{\mathrm{f}}(\mathbf{u}^{n+1}, p^{n+1}) + \boldsymbol{\mathcal{R}}(\mathbf{u}^{n+1}, \mathbf{u}_{\mathrm{ALE}}^{n+1}) = \mathbf{0} \end{aligned} & \text{in } \Omega_{\mathrm{f}} , \\[2mm] \nabla \cdot \mathbf{u}^{n+1} = 0 & \text{in } \Omega_{\mathrm{f}} , \\[2mm] \sigma_{\mathrm{f}}(\mathbf{u}^{n+1}, p^{n+1})\mathbf{n} = -\left(p_{\mathrm{VEN}}^{\mathrm{PUL}} \right)^{n+1} \mathbf{n} + \rho_{\mathrm{f}} \dfrac{\beta}{2}|\mathbf{u}^{n+1} \cdot \mathbf{n}|_{-}\mathbf{u}^{n+1} & \text{on } \Gamma_{\mathrm{f}}^{\mathrm{PV}} , \\[2mm] \sigma_{\mathrm{f}}(\mathbf{u}^{n+1}, p^{n+1})\mathbf{n} = -\left(p_{\mathrm{AR}}^{\mathrm{SYS}} \right)^{n+1} \mathbf{n} + \rho_{\mathrm{f}} \dfrac{\beta}{2}|\mathbf{u}^{n+1} \cdot \mathbf{n}|_{-}\mathbf{u}^{n+1} & \text{on } \Gamma_{\mathrm{f}}^{\mathrm{ao}} , \\[2mm] \mathbf{u}^{n+1} = \dfrac{\mathbf{d}^{n+1} - \mathbf{d}^n}{\Delta t} & \text{on } \Sigma , \\[2mm] \sigma_{\mathrm{f}}(\mathbf{u}^{n+1}, p^{n+1})\mathbf{n} = \sigma_{\mathrm{s}}(\mathbf{d}^{n+1}, \mathbf{s}^{n+1})\mathbf{n} & \text{on } \Sigma . \end{cases} \tag{12}$$

<div align="center">(a)   (b)   (c)</div>
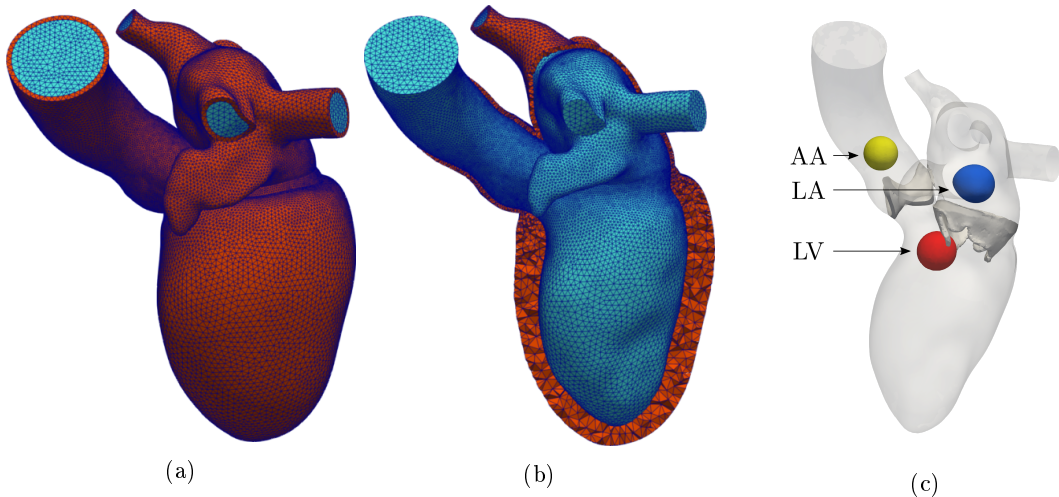
Figure 5: (a, b) Computational mesh used for the solid (red) and the fluid (blue) domains. (c) Spherical control volumes used in estimating the average pressures within each chamber. Average pressure within control volumes is also used to trigger the opening and closing of valves.

	$h_{\min}$[mm]	h_{avg}[mm]	$h_{\max}$[mm]	# **elem.**	# **nodes**
fluid	0.51	1.6	4.7	790 533	137 504
solid	0.59	2.1	5.7	234 132	63 834

Table 1: Minimum, average and maximum mesh element diameter, number of elements and number of nodes used for spatial discretization.

For our numerical simulations, we set $\Delta t = 0.2$ ms and $N_{\text{EP}} = 2$, so that $\Delta t_{\text{EP}} = 0.1$ ms.

3.2   Space discretization

We introduce a tetrahedral mesh in both domains $\widehat{\Omega}_{\text{s}}$ and $\widehat{\Omega}_{\text{f}}$, represented in Figures 5a and 5b. At their interface $\widehat{\Sigma}$, the fluid and solid meshes are conforming. The mesh $\widehat{\Omega}_{\text{f}}$ is updated following the displacement $\mathbf{d}_{\text{ALE}}$, resulting in a tetrahedral mesh over the domain Ω_{f}. The spatial discretization is finer in the region near the valves, to allow better capturing their presence. We report details about the mesh size and number of elements in Table 1.

The time-discrete ionic model (8) is solved at every vertex in the solid mesh. Then, ionic current $I_{\text{ion}}(v, \mathbf{w}, \mathbf{z})$ is evaluated at every mesh vertex, and interpolated on quadrature nodes of the mesh. This approach is referred to as *ionic current interpolation* (ICI) in the literature [82, 103].

We discretize in space the electrophysiology model (9) with piecewise quadratic finite elements [71, 108]. Indeed, quadratic finite elements have been shown to provide improved accuracy with a lower number of degrees of freedom, with respect to linear elements, for cardiac electrophysiology [3]. Since the ionic current term is known from the solution of the ionic model, the resulting problem is linear and symmetric. We solve it with the conjugate gradient (CG) method [108, 120], preconditioned with an algebraic multigrid (AMG) preconditioner [152]. We point out that, in principle, while we do not consider it in this work, a staggered scheme may allow to use a finer spatial discretization for the electrophysiology problem, e.g. by using intergrid transfer operators as presented in [122].

The system (10) is solved at every node in the computational mesh. The regularization problem (4) is solved by means of linear finite elements, using a regularization radius δ_{SL} proportional to the mesh size.
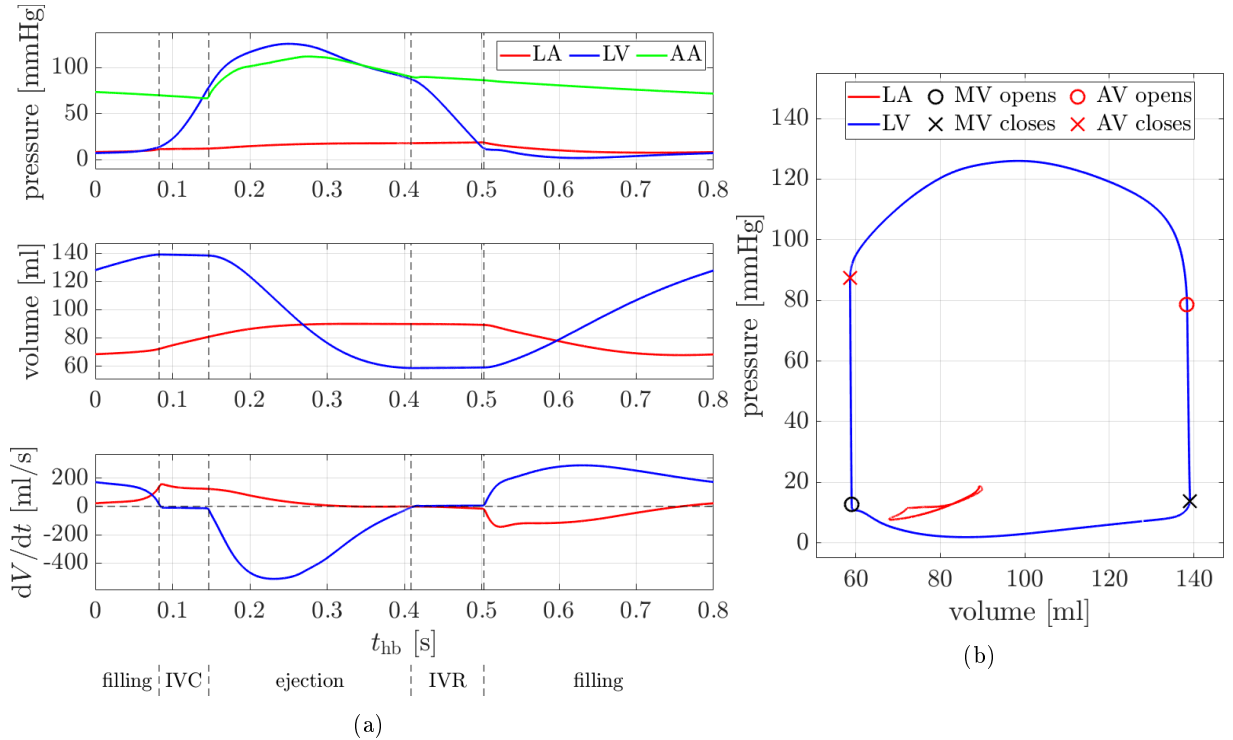
Figure 6: (a) Evolution, over the third simulated heartbeat, of the pressure p, volume V and volume derivative dV/dt for the left heart compartments. Vertical dashed lines separate heartbeat phases, labelled on the bottom. (b) Pressure-volume loops for the left ventricle and atrium, with marks indicating opening and closing of valves.

The resulting linear system is solved with the CG method, using AMG preconditioning.

The ALE lifting problem (11) is discretized in space with piecewise linear finite elements. The resulting problem is linearized with Newton's method and then solved with the GMRES method [108, 120], preconditioned with AMG.

The FSI problem (12) is discretized monolithically, using condensation of interface variables [22, 55, 97, 153]. We found that the monolithic approach is computationally more efficient and robust with respect to partitioned approaches based on subiterations between the fluid and the solid models, as detailed in [22]. Piecewise linear finite elements are used for the discretization of fluid velocity, fluid pressure and solild displacement. The use of VMS-LES model for the fluid equations yields a stable numerical solution even though linear finite element spaces for pressure and velocity do not fulfill the inf-sup condition [108]. The VMS-LES model also provides stabilization for the advection-dominated regime [13]. The resulting problem is linearized with Newton's method, and solved with the GMRES method, using a block lower-triangular preconditioner described in [22].

4   Numerical results

We run numerical simulations on a left heart model provided by Zygote Media Group [157], representing the heart of an average 21-year-old male. Preprocessing of the geometry was done using the algorithms presented in [47] as implemented in the software library `VMTK` [150]. Solvers for the individual core models and for the coupled model were implemented in the C++ library `life`$^\mathtt{x}$ [2, 1, 87], based on the finite element core

Indicator		Simulation	Normal values		Description
EDV	[mL]	139.1	126 to 208	[91]	left-ventricular end-diastolic volume
ESV	[mL]	58.6	35 to 80	[91]	left-ventricular end-systolic volume
SV	[mL]	80.4	81 to 137	[91]	left-ventricular stroke volume
EF	[%]	57.8	49 to 73	[27]	left-ventricular ejection fraction
$p_{\max}^{\text{LV}}$	[mmHg]	126.0	119±13	[133]	left-ventricular peak systolic pressure
$Q_{\max}^{\text{AV}}$	[mL/s]	510.0	427±129	[64]	peak-systolic aortic flow rate
T_{IVC}	[ms]	64.2	51 to 90	[44]	isovolumetric contraction time
T_{ej}	[ms]	261.0	230 to 334	[44]	ejection time
T_{IVR}	[ms]	94.2	50 to 140	[15]	isovolumetric relaxation time
T_{fil}	[ms]	379.0	280 to 472	[88]	diastolic filling time
LFS	[%]	17.8	13 to 21	[42]	longitudinal fractional shortening

Table 2: Values of physiological indicators computed from simulation results, and associated normal values from the medical literature. We report either normal ranges or mean ± standard deviation.

deal.II [6, 7, 34]. We run the simulations using 192 parallel processes on the GALILEO100 supercomputer[1] at the CINECA high-performance computing center (Italy).

We simulate three heartbeats, setting $T = 3T_{\text{hb}} = 2.4$ s, and consider only the last heartbeat in our analysis (starting at $t_0 = 2T_{\text{hb}} = 1.6$ s), to reduce the effect of initial conditions. We shall denote with $t_{\text{hb}} = t - t_0$ times relative to the third heartbeat.

For each heartbeat, the simulation takes approximately 21 h of wall time, of which 93 % is spent assembling and solving the FSI problem, 6 % assembling and solving the ALE lifting problem and 2 % assembling and solving the electrophysiology problem.

We found that the computational time associated to the ALE lifting is considerably higher using the non-linear problem (6) than using simpler harmonic or linear elastic lifting operators [131] (for which the wall time would be less than 1 % of the total). However, the latter frequently lead to mesh element inversion and solver breakdown, whereas the non-linear operator we employ has proven to be much more robust with respect to deformations.

For post-processing, we compute the average pressure of each compartment (LA, LV, AA) by averaging the pressure inside a spherical control volume within that compartment (see Figure 5c). In Figure 6, we report the average pressure, volume and volume derivative over time of the compartments. Table 2 collects some quantitative indicators for the heart function, comparing the values obtained by our simulation with data from the medical literature. Our numerical results are consistent with the clinically measured ranges. In the following sections, we provide details on the simulation results for each of the four heartbeat phases (identified in the plots of Figure 6).

4.1 Isovolumetric contraction

The heartbeat starts from the end of the diastolic filling phase, with the MV open and the AV closed (see Figure 6). The electrical stimulus is applied to the activation points of the left ventricle (see Section 2.2), leading to it being completely activated within $t_{\text{hb}} = 100$ ms (Figure 7a). This leads to the increase of intracellular calcium concentration (Figure 7d), which subsequently determines the generation of contractile force within the ventricular wall (Figure 7b). Intraventricular pressure rises, triggering the closure of the MV. When the valve is closed ($t_{\text{hb}} = 89$ ms), the ventricle is at its *end-diastolic volume* EDV = 139 mL.

---

[1]See https://wiki.u-gov.it/confluence/display/SCAIUS/UG3.3%3A+GALILEO100+UserGuide for technical specifications.
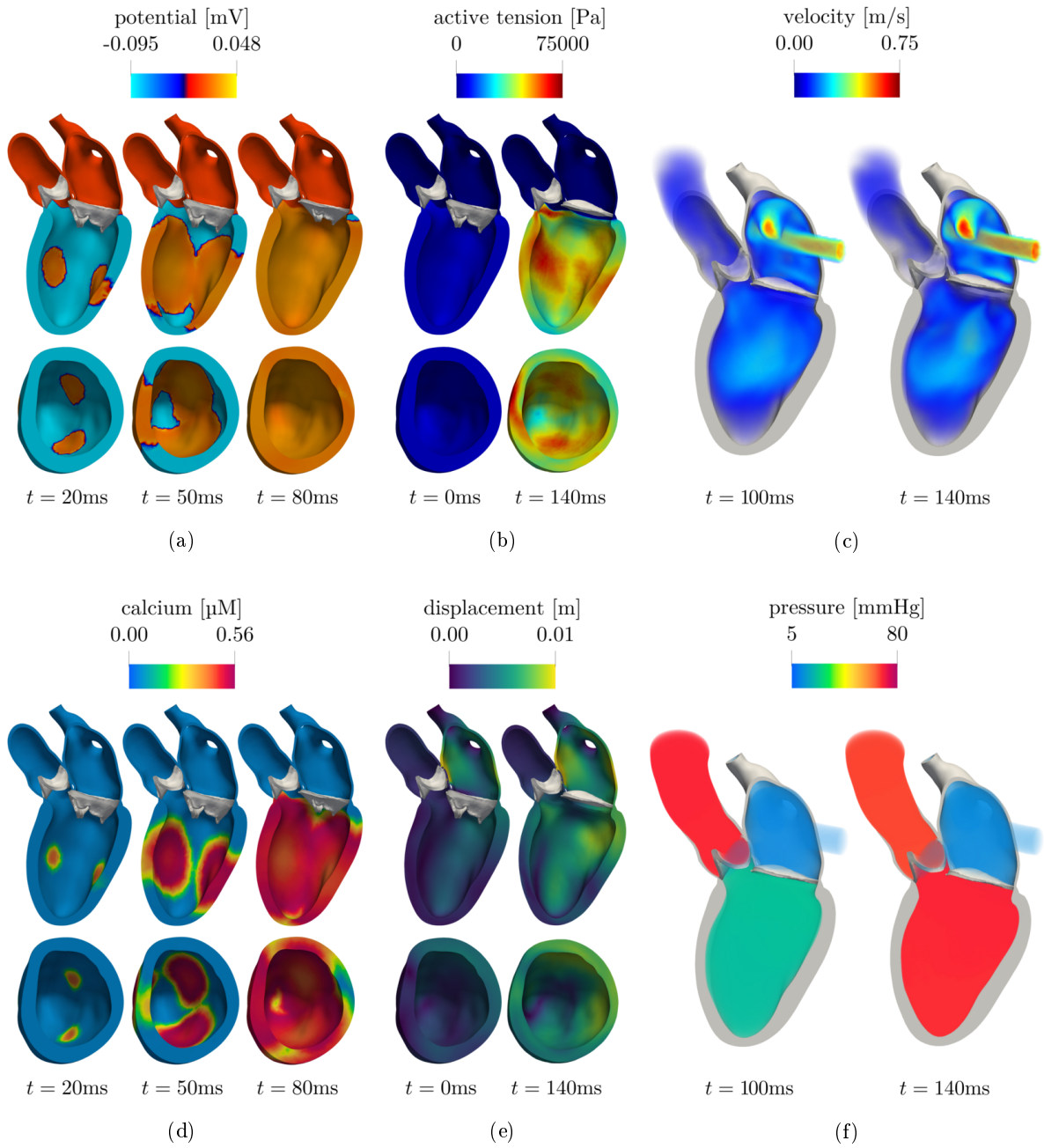
Figure 7: Solution snapshots during the isovolumetric contraction phase, as seen through a long-axis and a short-axis section: (a) transmembrane potential v; (b) active tension T_{act}; (c) volume rendering of the fluid velocity magnitude $|\mathbf{u}|$; (d) intracellular calcium concentration $[\mathrm{Ca}^{2+}]_{\mathrm{i}}$; (e) displacement magnitude $|\mathbf{d}|$; (f) volume rendering of the fluid pressure p.

17

At this point, the *isovolumetric contraction* (IVC) phase starts: both valves are closed, and the ventricular pressure increases rapidly (see Figure 6 and Figure 7f) while the volume is maintained approximately constant. Our model does not capture exactly the conservation of ventricular blood volume during this phase, due to the explicit discretization of the fluid domain displacement (11) and to the use of the resistive model for valves, which allows for a little flow through the immersed surfaces. Nonetheless, during isovolumetric contraction the maximum volume variation equals 0.7 mL, corresponding to 0.5 % of the EDV. We deem this spurious variation to be acceptable, in accordance with similar spurious variations observed in the cardiac modeling literature [147].

During the IVC phase, the ventricle undergoes a small deformation, with its shape becoming slightly more spherical (see Figures 7b and 7e) as described in [65, 79] .

The IVC phase lasts for $T_{\mathrm{IVC}} = 64.2$ ms, consistently with physiological behavior [44, 48]. When the pressure in the ventricle becomes larger than the pressure in the aorta, the opening of the AV is triggered and the ejection phase starts.

We remark that the possibility of including isovolumetric phases in a three-dimensional hemodynamics model is distinctive of FSI [22], as those phases cannot be represented by electromechanics-driven CFD models [156], unless ad-hoc techniques are implemented [139, 154].

4.2 Ejection

Blood is ejected from the ventricle into the aorta (Figure 8b). The maximum flow rate through the AV orifice is attained at $t_{\mathrm{hb}} = 231$ ms, and it equals $Q_{\max}^{\mathrm{AV}} = 510$ mL/s, consistently with physiology [62, 64]. It corresponds to an average velocity magnitude of $|\mathbf{u}|_{\max}^{\mathrm{AV}} = 1.46$ m/s on the AV section. The jet through the aortic valve is unsteady during all the ejection, consistently with the transitional nature of the flow (see Figure 8b). At the end of the ejection phase, the left ventricle attains its *end-systolic volume* ESV $= 58.6$ mL. Given EDV and ESV, we compute the *stroke volume* SV and *ejection fraction* EF as

$$\mathrm{SV} = \mathrm{EDV} - \mathrm{ESV} = 80.4\,\mathrm{mL} \qquad \mathrm{EF} = \frac{\mathrm{SV}}{\mathrm{EDV}} = 57.8\,\% \ .$$

Both quantities are within normal physiological ranges (see Table 2) [27, 48, 84, 91, 130].

During the ejection phase, the ventricular pressure increases until $t_{\mathrm{hb}} = 250$ ms, reaching a peak value of $p_{\max}^{\mathrm{LV}} = 126$ mmHg (see Figure 6), within the physiological ranges [79, 133]. After that, pressure starts decreasing until it falls below the aortic pressure, at which point the AV starts closing.

A similar evolution characterizes the pressure in the ascending aorta, reported in Figure 9: starting from an end-diastolic value of 68 mmHg, it reaches a peak of 112 mmHg and then declines until the next heartbeat. Although the absolute pressure values are smaller than normal ones [92], and there is a large pressure jump between the ventricle and the aorta (see Section 5), the time profile of the aortic pressure is remarkably similar to the ones obtained from in-vivo measurements [92, 94]. In particular, it features the *anacrotic notch*, resulting from the interaction of the forward and reflected pressure waves [94]. This effect is captured thanks to the FSI modeling framework, which, contrary to standalone CFD models, allows to obtain traveling pressure waves. The aortic pressure also features the *dicrotic notch* [79, 92, 130] in correspondence of the AV closure.

As the volume reduces, the ventricle becomes shorter and the atrioventricular plane shifts towards the ventricular apex (see Figure 10), as observed in healthy hearts [40, 79, 86]. We quantify this effect by computing the *longitudinal fractional shortening* (LFS) [86]: denoting by L_{ED} and L_{ES} the apico-basal distances at the end of diastole and at the end of systole, we have

$$\mathrm{LFS} = \frac{L_{\mathrm{ED}} - L_{\mathrm{ES}}}{L_{\mathrm{ED}}} = 17.8\,\% \ ,$$

which matches measurements on healthy hearts [42]. At the end of the systolic phase, the ventricular wall is approximately 14 % thicker than at the end of diastole [101].

During the late systolic phase, towards the end of the ejection, the ventricle repolarizes (Figure 11), with the transmembrane potential returning to its resting value.
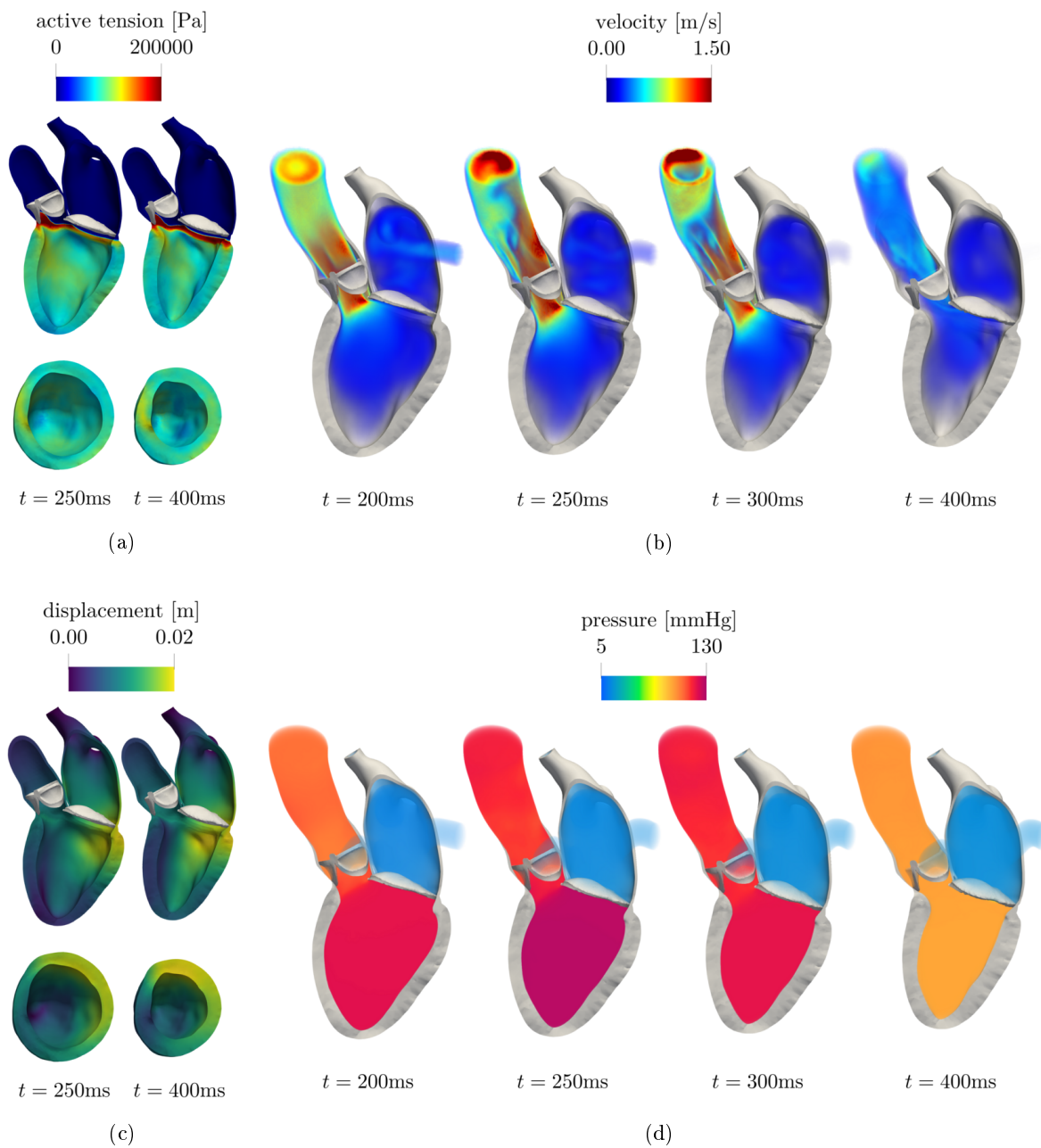
Figure 8: Solution snapshots during the ejection phase, as seen through a long-axis and a short-axis section: (a) active tension T_{act}; (b) volume rendering of the fluid velocity magnitude $|\mathbf{u}|$; (c) displacement magnitude $|\mathbf{d}|$; (d) volume rendering of the fluid pressure p.
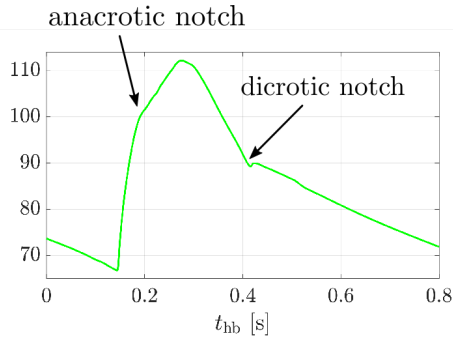
Figure 9: Average pressure in the ascending aorta over time. Notice the presence of the anacrotic notch during the systolic upstroke and of the dicrotic notch, or incisure, at the closing time of the AV.

Overall, the ejection phase lasts $T_{\text{ej}} = 261\,\text{ms}$, and the whole systolic phase lasts $T_{\text{sys}} = 326\,\text{ms}$, corresponding to $40.7\,\%$ of the heartbeat.

4.3 Isovolumetric relaxation

Once the AV is fully closed, the *isovolumetric relaxation* (IVR) phase starts (Figure 12). Ventricular pressure reduces as the ventricle relaxes at constant volume (Figure 6). This phase lasts for $T_{\text{IVR}} = 94.2\,\text{ms}$, consistently with physiology [15, 88], and the MV starts opening as soon as the ventricular pressure becomes smaller than the atrial pressure.

As observed for the IVC phase, our model features a small spurious variation in volume during isovolumetric phases. In the case of the IVR phase, the variation amounts to $0.4\,\text{mL}$, corresponding to $0.6\,\%$ of the ESV. Also in this case, we deem the spurious variation to be acceptable.

4.4 Filling

Once the MV is open, blood flows from the atrium into the ventricle (Figure 13b). The flow is characterized by the formation of a jet through the MV, that is associated to a vortex ring (Figure 14a). The vortex ultimately dissipates near to the ventricular free wall, while becoming larger near the septum (Figures 14b and 14c) resulting in a single vortex that rotates clockwise, if observed from a long-axis view with the septum on the left. This behavior is observed in medical images of healthy hearts [37, 104]. At the same time, the atrioventricular plane shifts towards the atrium, while the ventricular volume increases. Since our model does not account for atrial contraction, the simulated diastolic phase lacks the atrial kick [79]. This also determines higher-than-normal pressure and volume in the left atrium (with a peak pressure of $19\,\text{mmHg}$, against a normal value of about $8\,\text{mmHg}$) [48]. Filling continues until the ventricle starts contracting again, leading to the closure of the MV and the beginning of a new cardiac cycle. The filling phase lasts for $T_{\text{fil}} = 379\,\text{ms}$, and the whole diastolic phase lasts for $T_{\text{dia}} = 474\,\text{ms}$, corresponding to $59.3\,\%$ of the heartbeat.

4.5 Conservation of blood volume

The explicit treatment of the geometric FSI coupling condition and of the coupling between the Navier-Stokes equations and the circulation model might in principle lead to variations over time in the total blood volume. To assess whether this has an impact on simulation results, we compute the total blood volume over time as follows:

$$V_{\text{tot}}(t) = V_{\text{VEN}}^{\text{PUL}}(t) + V^{\text{LA}}(t) + V^{\text{LV}}(t) + V_{\text{AR}}^{\text{SYS}}(t) + V_{\text{VEN}}^{\text{SYS}}(t) + V_{\text{RA}}(t) + V_{\text{RV}}(t) + V_{\text{AR}}^{\text{PUL}}(t) \, ,$$
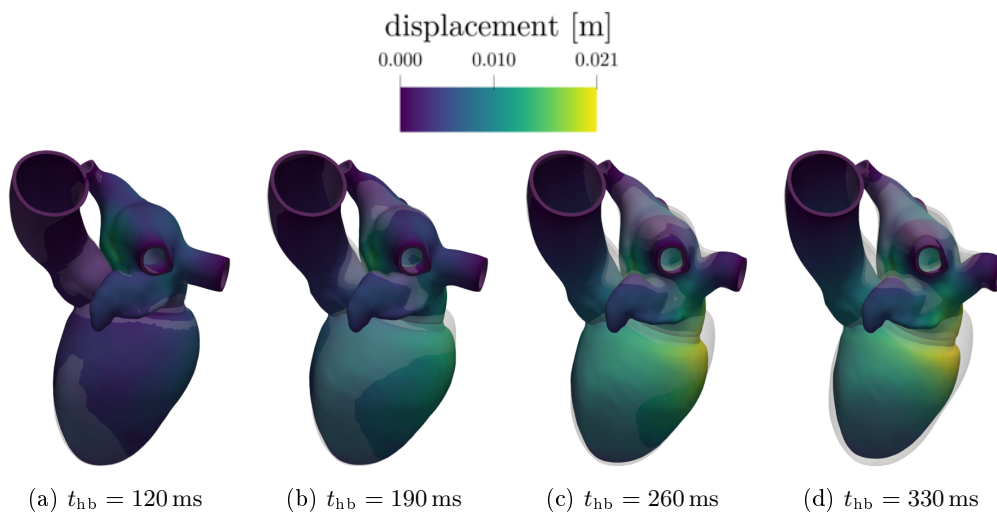
20

Figure 10: Magnitude of the displacement **d** at four instants during the ejection phase. The initial configuration is overlaid in trasparency, and the domain is warped by **d**. Notice how the ventricle becomes shorter during the ejection, mostly due to the shift of the atrioventricular plane towards the apex.
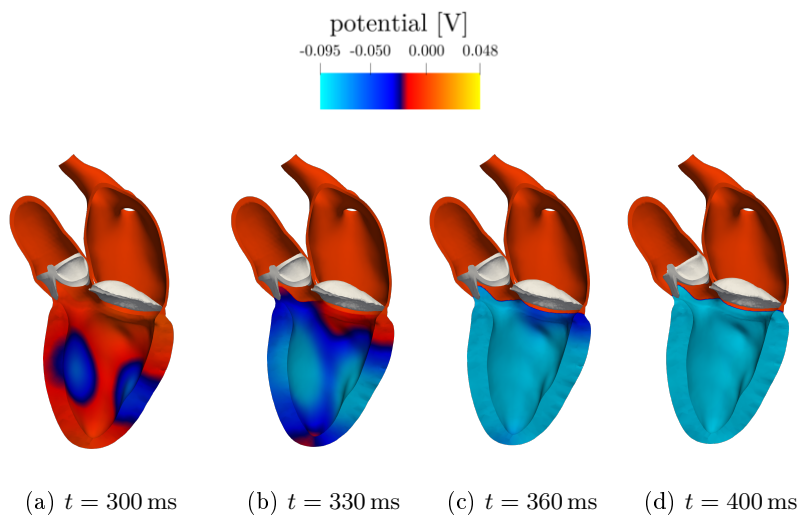

Figure 11: Repolarization of the left ventricle. The ventricular transmembrane potential gradually returns to its resting value.
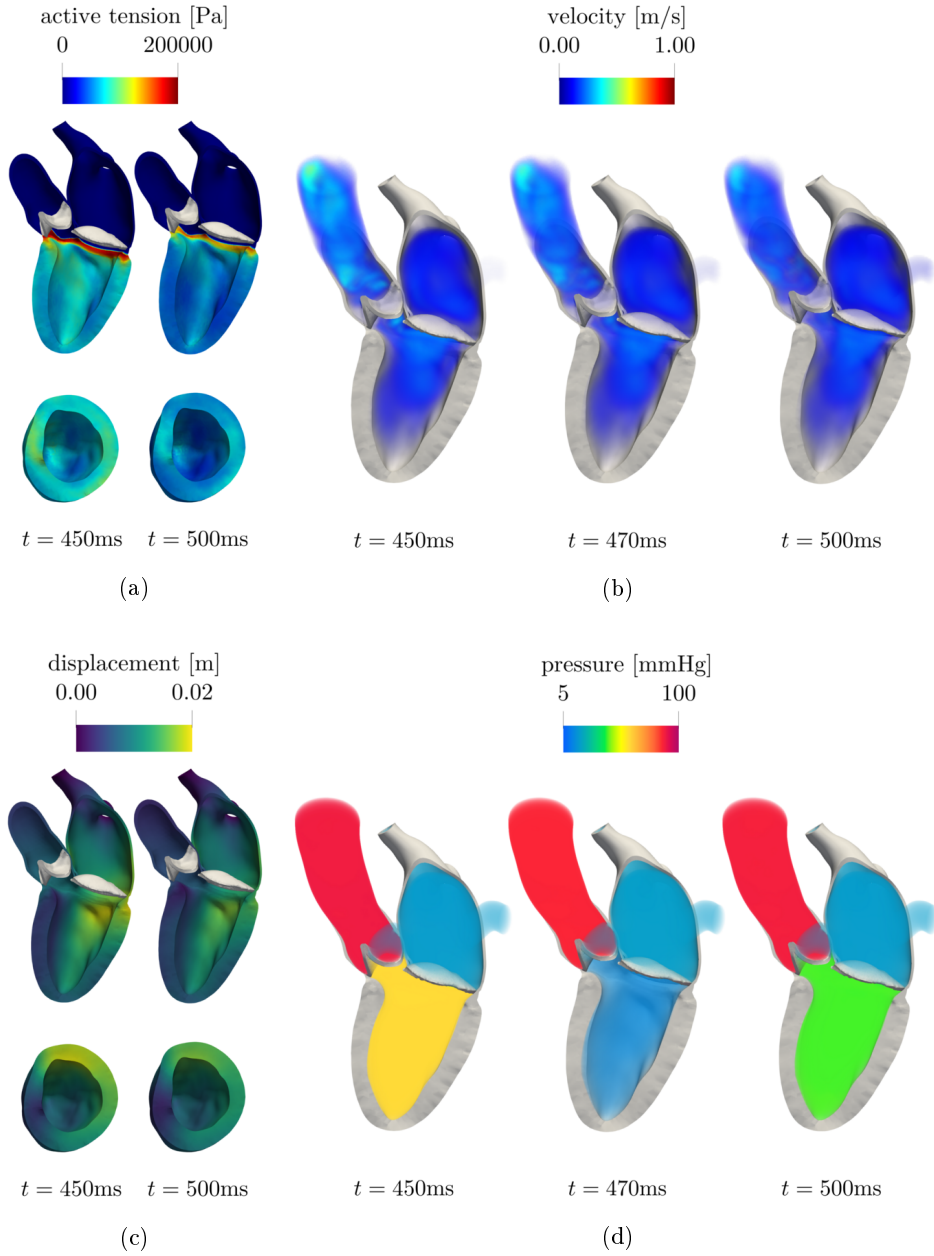
Figure 12: Solution snapshots during the isovolumetric relaxation phase, as seen through a long-axis and a short-axis section: (a) active tension T_{act}; (b) volume rendering of the fluid velocity magnitude $|\mathbf{u}|$; (c) displacement magnitude $|\mathbf{d}|$; (d) volume rendering of the fluid pressure p.

Figure 13: Solution snapshots during the filling phase, as seen through a long-axis and a short-axis section: (a) active tension T_{act}; (b) volume rendering of the fluid velocity magnitude $|\mathbf{u}|$; (c) displacement magnitude $|\mathbf{d}|$; (d) volume rendering of the fluid pressure p.
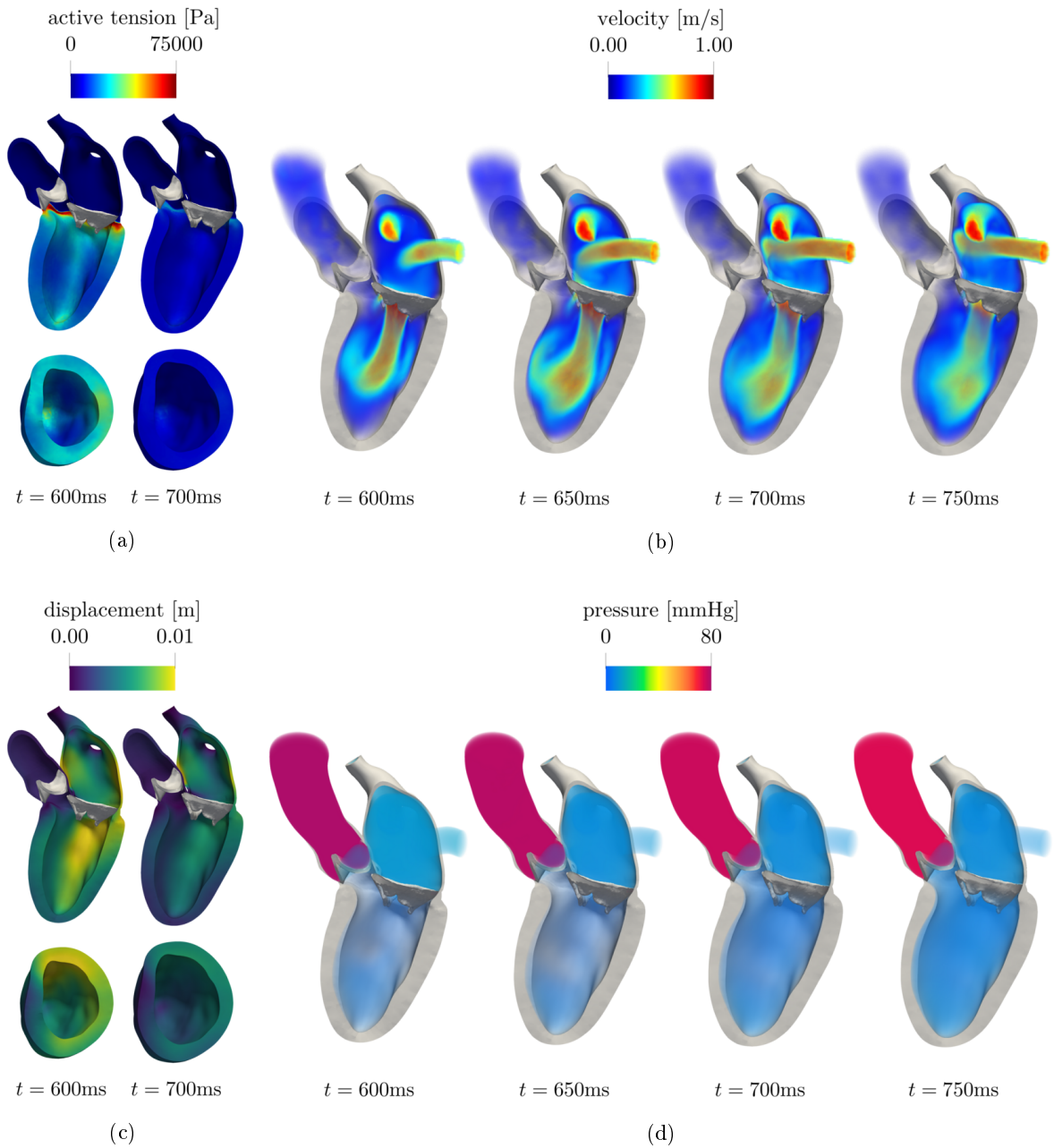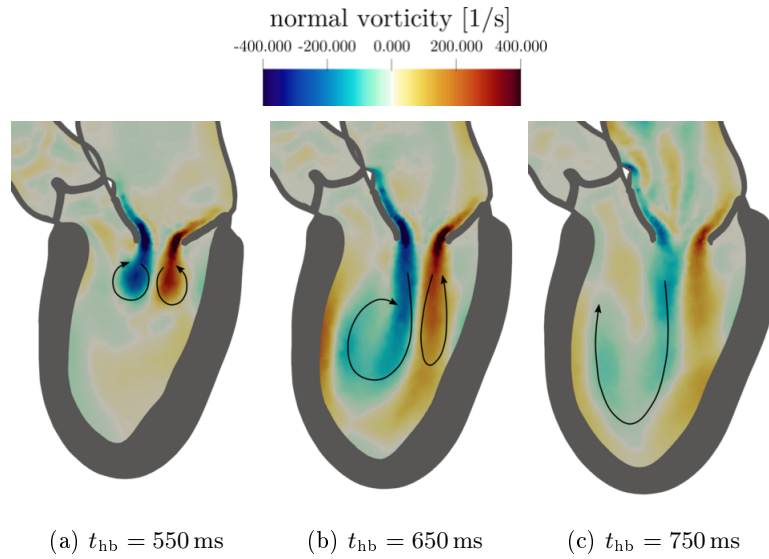
23

(a) $t_{\mathrm{hb}} = 550\,\mathrm{ms}$ (b) $t_{\mathrm{hb}} = 650\,\mathrm{ms}$ (c) $t_{\mathrm{hb}} = 750\,\mathrm{ms}$

Figure 14: Vorticity $\mathbf{w}\cdot\mathbf{N} = (\nabla \times \mathbf{u})\cdot\mathbf{N}$ of the velocity field, projected onto a slice of the domain (with normal $\mathbf{N}$ pointing outwards from the slice plane). The arrows indicate the direction of the rotating vortices.
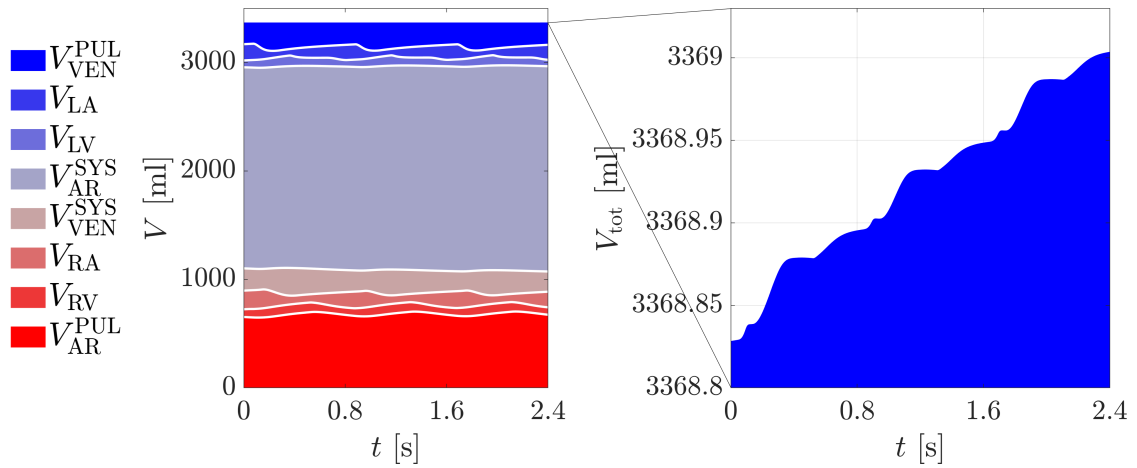

Figure 15: Blood volume over three heartbeats in each compartment of the heart and circulation. The zoom on the right shows how the total blood volume exhibits a very small variation in time: the mass gain over three heartbeats is only 0.0052 % of the total.

where $V^{LA}(t)$ and $V^{LV}(t)$ are the volumes of Ω^{LA} and $\Omega^{LV} \cup \Omega^{ring}$ at time t, respectively, and

$$V_{AR}^{SYS}(t) = V_{AR,0}^{SYS} + V^{AA}(t) + C_{AR}^{SYS}(p_{AR}^{SYS}(t) - p_{EX}(t)) \,,$$
$$V_{VEN}^{SYS}(t) = V_{VEN,0}^{SYS} + C_{VEN}^{SYS}(p_{VEN}^{SYS}(t) - p_{EX}(t)) \,,$$
$$V_{AR}^{PUL}(t) = V_{AR,0}^{PUL} + C_{AR}^{PUL}(p_{AR}^{PUL}(t) - p_{EX}(t)) \,,$$
$$V_{VEN}^{PUL}(t) = V_{VEN,0}^{PUL} + C_{VEN}^{PUL}(p_{VEN}^{PUL}(t) - p_{EX}(t)) \,.$$

The latter equations are obtained by integrating the respective equations of the circulation model. We assume the zero-pressure volumes $V_{j,0}^i$ to be zero for simplicity, since they are constant in time and do not influence the assessment of blood volume conservation.

We report the blood volume over time for the different compartments, as well as the total blood volume, in Figure 15. From there, we can appreciate how the distribution of blood between the different compartments varies over time, but the total volume remains approximately constant. Indeed, the range of variation of the total volume over the three simulated heartbeats equals

$$\frac{\max_{t \in (0,T)} V_{tot}(t) - \min_{t \in (0,T)} V_{tot}(t)}{\max_{t \in (0,T)} V_{tot}(t)} = 0.0052 \,\% \,.$$

We deem this very small variation over three heartbeats to be negligible and the result highly accurate. Therefore, the approximation introduced by the explicit discretization of geometric FSI coupling and circulation coupling does not introduce significant errors in terms of mass conservation.

5   Limitations of the current study

In this section we present some limitations associated to the proposed computational framework, related to modeling choices and simplifications. To begin with, we modeled the LA as passive from both the electrical and mechanical viewpoints, for simplicity. On the contrary, in real hearts the left atrium is electrically active and contracts at the end of the diastolic phase, providing extra preload to the left ventricle along with an additional jet through the MV [79, 81]. The inclusion of suitable atrial electromechanical models will be the subject of future studies.

The stimulation protocol used to trigger the activation of the myocardium is simplified if compared to the behavior of the cardiac conduction system [32, 36, 85, 79, 118, 143]. While this simplification is acceptable in physiological conditions [115], more detailed models might yield better descriptions of the ventricular activation pattern, which can become especially relevant if pathological scenarios are considered.

We employed the RIIS model for valve dynamics, prescribing the kinematics of the valve and neglecting any dynamic interaction with the blood. Moreover, we displace the valves along with the fluid domain displacement $\mathbf{d}_{ALE}$, which has no physical meaning. Valve FSI plays a major role in the blood dynamics [41, 49, 50, 70, 89, 90, 138], as well as being responsible for several pathologies of clinical interest [30, 33]. While in this work we are mostly interested on the macroscopic effect of valves on the blood flow, the incorporation of suitable FSI models of the valves will be the subject of future studies.

Finally, in terms of numerical results, one major mismatch between our model and physiological data is the pressure difference between the ventricle and the aorta during the ejection phase. We obtain a maximum pressure difference of $18 \,\mathrm{mmHg}$. Such a high value, although not uncommon in the cardiac modeling literature [139, 147], is typically associated with a stenotic valve in clinical measurements [75, 151]. We believe this to be caused by minor inconsistencies in the geometrical model (based on a template obtained averaging over a sample of people, rather than on a specific individual) and by the simplicity of the valve model considered In any case, further investigations on this point are in order.

6   Conclusions

We introduced a novel fully integrated computational framework for the modeling and simulation of the human heart. The proposed model features three-dimensional and highly detailed descriptions of electro-

physiology, active and passive mechanics and blood dynamics, as well as reduced models for valves and circulation. We included feedback effects among the different core models, resulting in a coupled multi-physics and multiscale problem.

Suitable numerical techniques were presented with the aim of solving efficiently the model equations. In particular, a staggered scheme with respect to time allowed for a flexible and efficient solution. Numerical methods were implemented in a high-performance computing framework within the `life`ˣ library. We simulated a human left heart, and the results indicate that the proposed computational framework has the potential of describing accurately the physics of the heart, accounting for multiple feedback effects and overall capturing the interplay between the different processes driving the heartbeat. Our model is capable of representing all phases of the heartbeat and their durations, in accordance with clinical data. Moreover, through the coupling with a closed-loop circulation model, we were able to account for the interplay between the heart and the circulatory system, and guarantee the total blood volume conservation in time. The model correctly represents isovolumetric phases of the heartbeat, and reproduces effects associated to traveling pressure waves, thanks to the FSI coupling, suggesting that an EMF coupled modeling framework can overcome some of the limitations of electromechanics-driven CFD simulations. A more systematic comparison of the two modeling approaches will be the subject of future studies.

The agreement between numerical results and biomarkers from the medical literature suggests that the proposed model can be used for the investigation of the physiological cardiac function as well as for the simulation of pathological scenarios, and can serve as a stepping stone towards realistic and accurate integrated models of the whole heart.

7 Acknowledgements

A Solid mechanics constitutive laws

The Guccione strain energy is computed from the displacement $\mathbf{d}$ as [61]

$$\mathcal{W}_{\mathrm{G}}(\mathbf{d}) = \frac{c}{2}\left(\exp(Q) - 1\right) + \frac{\kappa}{2}(J-1)\log(J),$$

where

$$Q = \sum_{\mathrm{i,j} \in \{\mathrm{f,s,n}\}} a_{\mathrm{i,j}} \left(E\mathbf{j} \cdot \mathbf{i}\right)^2 \ ,$$

$$E = \frac{1}{2} \left(F^T F - I\right) \ .$$

The strain energy function associated to the neo-Hookean model is given by [98]

$$\mathcal{W}_{\mathrm{NH}}(\mathbf{d}) = \frac{\mu}{2} \left(J^{-\frac{2}{3}} F : F - 3\right) + \frac{\kappa}{4} \left((J-1)^2 + \log^2(J)\right) \ .$$

The values of the constant parameters appearing in both constitutive laws are reported in Appendix D.

B Valve modeling

The heart model includes the MV in open configuration $\Gamma_{\mathrm{MV}}^{\mathrm{open}}$ and the AV in closed configuration $\Gamma_{\mathrm{AV}}^{\mathrm{closed}}$. The opposite configurations, $\Gamma_{\mathrm{MV}}^{\mathrm{closed}}$ and $\Gamma_{\mathrm{AV}}^{\mathrm{open}}$, are obtained in a preprocessing step as described in [156]. The procedure also yields the displacement vectors between the two configurations, that is two fields $\mathbf{d}_{\mathrm{k}}$: $\Gamma_{\mathrm{k}}^{\mathrm{closed}} \to \mathbb{R}^3$ such that

$$\Gamma_{\mathrm{k}}^{\mathrm{open}} = \left\{\mathbf{x}^{\mathrm{open}} \in \Omega_{\mathrm{f}} \colon \mathbf{x}^{\mathrm{open}} = \mathbf{x}^{\mathrm{closed}} + \mathbf{d}_{\mathrm{k}}(\mathbf{x}^{\mathrm{closed}}), \ \mathbf{x}^{\mathrm{closed}} \in \Gamma_{\mathrm{k}}^{\mathrm{closed}}\right\} \ .$$

Then, at any time $t \in (0, T)$ the configuration Γ_{k}^t of the valve is given by

$$\Gamma_{\mathrm{k}}^{\mathrm{t}} = \left\{\mathbf{x}^{\mathrm{t}} = \mathbf{x}^{\mathrm{closed}} + c_{\mathrm{k}}(t)\,\mathbf{d}_{\mathrm{k}}(\mathbf{x}^{\mathrm{closed}}) + \mathbf{d}_{\mathrm{ALE}}(\mathbf{x}^{\mathrm{closed}}, t), \ \mathbf{x}^{\mathrm{closed}} \in \Gamma_{\mathrm{k}}^{\mathrm{closed}}\right\} \ ,$$

wherein $c_{\mathrm{k}}(t)$ is a time-dependent opening coefficient that is equal to 0 when the valve is fully closed and to 1 when it is fully open. The functions $c_{\mathrm{k}}(t)$ are prescribed a priori, in the form

$$c_{\mathrm{k}}(t) = \begin{cases} 0 & \text{if } t \leq t_{\mathrm{k}}^{\mathrm{open}} \ , \\ \frac{1}{2} \left(1 - \cos\left(\pi \dfrac{1 - \exp\{-\chi_{\mathrm{k}}(t - t_{\mathrm{k}}^{\mathrm{open}})/\Delta t_{\mathrm{k}}^{\mathrm{open}}\}}{1 - \exp(-\chi_{\mathrm{k}})}\right)\right) & \text{if } t_{\mathrm{k}}^{\mathrm{open}} < t \leq t_{\mathrm{k}}^{\mathrm{open}} + \Delta t_{\mathrm{k}}^{\mathrm{open}} \ , \\ 1 & \text{if } t_{\mathrm{k}}^{\mathrm{open}} + \Delta t_{\mathrm{k}}^{\mathrm{open}} < t < t_{\mathrm{k}}^{\mathrm{close}} \ , \\ 1 - \frac{1}{2} \left(1 - \cos\left(\pi \dfrac{1 - \exp\{-\chi_{\mathrm{k}}(t - t_{\mathrm{k}}^{\mathrm{close}})/\Delta t_{\mathrm{k}}^{\mathrm{close}}\}}{1 - \exp(-\chi_{\mathrm{k}})}\right)\right) & \text{if } t_{\mathrm{k}}^{\mathrm{close}} < t \leq t_{\mathrm{k}}^{\mathrm{close}} + \Delta t_{\mathrm{k}}^{\mathrm{close}} \ , \\ 0 & \text{if } t > t_{\mathrm{k}}^{\mathrm{close}} + \Delta t_{\mathrm{k}}^{\mathrm{close}} \ . \end{cases}$$

The parameters p_{k}, $\Delta t_{\mathrm{k}}^{\mathrm{open}}$ and $\Delta t_{\mathrm{k}}^{\mathrm{close}}$ are prescribed and they determine the opening speed of the valve. The opening time $t_{\mathrm{k}}^{\mathrm{open}}$ is the first instant at which the difference between upstream and downstream pressures is positive, while the closing time $t_{\mathrm{k}}^{\mathrm{close}}$ is the first instant at which the pressure difference is negative. Pressure difference is evaluated averaging over spherical control volumes as in [156] (see Figure 5c).

We remark that we displace the valves following the fluid domain. Moreover, we take $\mathbf{u}_{\Gamma_{\mathrm{k}}} = \mathbf{0}$, i.e. we neglect the valve velocity due to the change of its configuration. This corresponds to a quasi-static approximation of the valve opening and closing [45].

C Blood circulation model

The equations for the blood circulation model read: for $t \in (0, T)$,

$$\begin{cases} C_{\mathrm{AR}}^{\mathrm{SYS}} \dfrac{\mathrm{d}p_{\mathrm{AR}}^{\mathrm{SYS}}(t)}{\mathrm{d}t} = Q_{\mathrm{AV}}(t) - Q_{\mathrm{AR}}^{\mathrm{SYS}}(t) \,, \\[2mm] \dfrac{L_{\mathrm{AR}}^{\mathrm{SYS}}}{R_{\mathrm{AR}}^{\mathrm{SYS}}} \dfrac{\mathrm{d}Q_{\mathrm{AR}}^{\mathrm{SYS}}(t)}{\mathrm{d}t} = -Q_{\mathrm{AR}}^{\mathrm{SYS}}(t) - \dfrac{p_{\mathrm{VEN}}^{\mathrm{SYS}}(t) - p_{\mathrm{AR}}^{\mathrm{SYS}}(t)}{R_{\mathrm{AR}}^{\mathrm{SYS}}} \,, \\[2mm] C_{\mathrm{VEN}}^{\mathrm{SYS}} \dfrac{\mathrm{d}p_{\mathrm{VEN}}^{\mathrm{SYS}}(t)}{\mathrm{d}t} = Q_{\mathrm{AR}}^{\mathrm{SYS}}(t) - Q_{\mathrm{VEN}}^{\mathrm{SYS}}(t) \,, \\[2mm] \dfrac{L_{\mathrm{VEN}}^{\mathrm{SYS}}}{R_{\mathrm{VEN}}^{\mathrm{SYS}}} \dfrac{\mathrm{d}Q_{\mathrm{VEN}}^{\mathrm{SYS}}(t)}{\mathrm{d}t} = -Q_{\mathrm{VEN}}^{\mathrm{SYS}}(t) - \dfrac{p_{\mathrm{RA}}(t) - p_{\mathrm{VEN}}^{\mathrm{SYS}}(t)}{R_{\mathrm{AR}}^{\mathrm{SYS}}} \,, \\[2mm] p_{\mathrm{RA}}(t) = p_{\mathrm{EX}}(t) + E_{\mathrm{RA}}(t)(V_{\mathrm{RA}}(t) - V_{0,\mathrm{RA}}) \,, \\[2mm] \dfrac{\mathrm{d}V_{\mathrm{RA}}(t)}{\mathrm{d}t} = Q_{\mathrm{VEN}}^{\mathrm{SYS}}(t) - Q_{\mathrm{TV}}(t) \,, \\[2mm] Q_{\mathrm{TV}}(t) = \dfrac{p_{\mathrm{RA}}(t) - p_{\mathrm{RV}}(t)}{R_{\mathrm{TV}}(p_{\mathrm{RA}}(t), p_{\mathrm{RV}}(t))} \,, \\[2mm] p_{\mathrm{RV}}(t) = p_{\mathrm{EX}}(t) + E_{\mathrm{RV}}(t)(V_{\mathrm{RV}}(t) - V_{0,\mathrm{RV}}) \,, \\[2mm] \dfrac{\mathrm{d}V_{\mathrm{RV}}(t)}{\mathrm{d}t} = Q_{\mathrm{TV}}(t) - Q_{\mathrm{PV}}(t) \,, \\[2mm] Q_{\mathrm{PV}}(t) = \dfrac{p_{\mathrm{RV}}(t) - p_{\mathrm{AR}}^{\mathrm{PUL}}(t)}{R_{\mathrm{PV}}(p_{\mathrm{RV}}(t), p_{\mathrm{AR}}^{\mathrm{PUL}}(t))} \,, \\[2mm] C_{\mathrm{AR}}^{\mathrm{PUL}} \dfrac{\mathrm{d}p_{\mathrm{AR}}^{\mathrm{PUL}}(t)}{\mathrm{d}t} = Q_{\mathrm{PV}}(t) - Q_{\mathrm{AR}}^{\mathrm{PUL}}(t) \,, \\[2mm] \dfrac{L_{\mathrm{AR}}^{\mathrm{PUL}}}{R_{\mathrm{AR}}^{\mathrm{PUL}}} \dfrac{\mathrm{d}Q_{\mathrm{AR}}^{\mathrm{PUL}}(t)}{\mathrm{d}t} = -Q_{\mathrm{AR}}^{\mathrm{PUL}}(t) - \dfrac{p_{\mathrm{VEN}}^{\mathrm{PUL}}(t) - p_{\mathrm{AR}}^{\mathrm{PUL}}(t)}{R_{\mathrm{AR}}^{\mathrm{PUL}}} \,, \\[2mm] C_{\mathrm{VEN}}^{\mathrm{PUL}} \dfrac{\mathrm{d}p_{\mathrm{VEN}}^{\mathrm{PUL}}(t)}{\mathrm{d}t} = Q_{\mathrm{AR}}^{\mathrm{PUL}}(t) - Q_{\mathrm{VEN}}^{\mathrm{PUL}}(t) \,, \\[2mm] p_{\mathrm{LA}}^{\mathrm{in}}(t) = p_{\mathrm{VEN}}^{\mathrm{PUL}}(t) - R_{\mathrm{VEN}}^{\mathrm{PUL}} Q_{\mathrm{VEN}}^{\mathrm{PUL}}(t) - L \dfrac{\mathrm{d}Q_{\mathrm{VEN}}^{\mathrm{PUL}}(t)}{\mathrm{d}t} \,, \end{cases} \tag{13}$$

endowed with suitable initial conditions. In the above system, $p_{\mathrm{EX}}(t) = 0$ represents an external pressure, $E_{\mathrm{RA}}(t)$ and $E_{\mathrm{RV}}(t)$ are time-varying elastances modeling the contraction of the right atrium and ventricle, defined as

$$E_{\mathrm{i}}(t) = E_{\mathrm{i}}^{\mathrm{B}} + E_{\mathrm{i}}^{\mathrm{B}} \varphi_{\mathrm{act}}(t, t_{\mathrm{c}}^{\mathrm{i}}, T_{\mathrm{c}}^{\mathrm{i}}, T_{\mathrm{r}}^{\mathrm{i}}) \,,$$

φ_{act} is defined as in [115], and $V_{0,\mathrm{RA}}$ and $V_{0,\mathrm{RV}}$ are the resting volumes of left atrium and ventricle. Valvular resistances R_{TV} and R_{PV} are given by

$$R_{\mathrm{k}}(p_1, p_2) = \begin{cases} R_{\max} & \text{if } p_1 < p_2 \,, \\ R_{\min} & \text{if } p_1 \geq p_2 \,, \end{cases} \qquad \mathrm{k} \in \{\mathrm{TV}, \mathrm{PV}\} \,.$$

The rest of the resistances, capacitances and inductances are parameters surrogating the properties of the circulation network.

D Model parameters

We report a list of the parameters used for the simulation described in Section 4. Table 3 reports parameters for the electrophysiology model, Table 4 those for the force generation model, Table 5 those for the solid

	Parameter	Value	
Monodomain	χ	1400	1/cm
	C_{m}	1	$\mathrm{\mu F/cm^2}$
Conductivities	$\sigma_{\mathrm{m}}^{\mathrm{l}}/(\chi C_{\mathrm{m}})$	2.00×10^{-4}	$\mathrm{m^2/s}$
	$\sigma_{\mathrm{m}}^{\mathrm{t}}/(\chi C_{\mathrm{m}})$	1.05×10^{-4}	$\mathrm{m^2/s}$
	$\sigma_{\mathrm{m}}^{\mathrm{n}}/(\chi C_{\mathrm{m}})$	0.55×10^{-4}	$\mathrm{m^2/s}$
Stimulus	$A_{\mathrm{app}}/C_{\mathrm{m}}$	25.71	V/s
	σ_{app}	2.5×10^{-3}	m
	T_{app}	3	ms

Table 3: Parameters used in the electrophysiology model. Conductivities were tuned so as to obtain a conduction velocity of 0.6 m/s, 0.4 m/s and 0.2 m/s along fibers, sheets and normal-to-fiber directions, respectively. The parameters used for the ionic model are those of the original paper [136].

Parameter	Value	
γ	30	
k_d	0.36	
α_{k_d}	-0.2083	
K_{off}	8	1/s
K_{basic}	4	1/s
μ_{fp}^0	32.255	1/s
μ_{fp}^1	0.768	1/s
a_{XB}	8.9491×10^8	Pa
SL_0	2.1	$\mathrm{\mu m}$

Table 4: Parameters used in the force generation model. We only report those parameters whose values differ from the original setting described in [113].

mechanics model, Table 6 lists the parameters used in the fluid dynamics model and Tables 7 and 8 those of the circulation model. For the RDQ20-MF force generation model, we only report those parameters whose values differ from those presented in [113]. We refer the interested reader to [136] for details on the parameters of the TTP06 ionic model.

Parameter		Value	
	ρ_{s}	1000	$\mathrm{kg/m^2}$
Guccione (atrium and ventricle)	c	8.8×10^2	Pa
	a_{ff}	8	
	a_{ss}	6	
	a_{nn}	3	
	a_{fs}	12	
	a_{fn}	3	
	a_{sn}	3	
	κ	5×10^4	Pa
Atrioventricular ring	μ	5×10^6	Pa
	κ	1×10^6	Pa
Ascending aorta	μ	5.25×10^5	Pa
	κ	1×10^6	Pa
Boundary conditions	$K_{\perp}^{\mathrm{epi}}$	2×10^5	Pa/m
	$K_{\parallel}^{\mathrm{epi}}$	2×10^4	Pa/m
	$C_{\perp}^{\mathrm{epi}}$	2×10^4	$\mathrm{Pa \cdot s/m}$
	$C_{\parallel}^{\mathrm{epi}}$	2×10^3	$\mathrm{Pa \cdot s/m}$
Initial conditions	p_0^{LA}	9.75	mmHg
	p_0^{ring}	11.25	mmHg
	p_0^{LV}	11.25	mmHg
	p_0^{AA}	80	mmHg
Interface regularization	$\psi_{\mathrm{th}}^{\mathrm{LV}}$	0.2	
	$\psi_{\mathrm{th}}^{\mathrm{LA}}$	0.1	

Table 5: Parameters used in the solid mechanics model.

	Parameter	Value	
Navier-Stokes	ρ_{f}	1060	$\mathrm{kg/m^3}$
	μ_{f}	3.5×10^{-3}	$\mathrm{Pa \cdot s}$
Valve modeling	$R_{\mathrm{MV}},\ R_{\mathrm{AV}}$	1×10^5	$\mathrm{kg/(m \cdot s)}$
	$\varepsilon_{\mathrm{MV}},\ \varepsilon_{\mathrm{AV}}$	0.75×10^{-3}	m
	$\Delta t_{\mathrm{MV}}^{\mathrm{open}}$	10	ms
	$\Delta t_{\mathrm{AV}}^{\mathrm{open}}$	10	ms
	$\Delta t_{\mathrm{MV}}^{\mathrm{close}}$	30	ms
	$\Delta t_{\mathrm{AV}}^{\mathrm{close}}$	80	ms
	$\chi_{\mathrm{MV}},\ \chi_{\mathrm{AV}}$	-3	

Table 6: Parameters used in the fluid dynamics model. Valve half-thicknesses $\varepsilon_{\mathrm{MV}}$ and $\varepsilon_{\mathrm{AV}}$ were chosen to match literature data [41, 121]. Resistances $R_{\mathrm{MV}},\ R_{\mathrm{AV}}$ were chosen to be sufficiently high to guarantee minimal spurious flow through valves without hindering the conditioning of the FSI system.

	Parameter	Value	
Systemic arteries	$R_{\mathrm{AR}}^{\mathrm{SYS}}$	0.45	$\mathrm{mmHg \cdot s/mL}$
	$C_{\mathrm{AR}}^{\mathrm{SYS}}$	2.19	$\mathrm{mL/mmHg}$
	$L_{\mathrm{AR}}^{\mathrm{SYS}}$	2.7×10^{-3}	$\mathrm{mmHg \cdot s^2/mL}$
	$R_{\mathrm{upstream}}^{\mathrm{SYS}}$	0.07	$\mathrm{mmHg \cdot s/mL}$
	$p_{\mathrm{AR}}^{\mathrm{SYS}}(0)$	80	mmHg
	$Q_{\mathrm{AR}}^{\mathrm{SYS}}(0)$	66.5775	mL/s
Systemic veins	$R_{\mathrm{VEN}}^{\mathrm{SYS}}$	0.26	$\mathrm{mmHg \cdot s/mL}$
	$C_{\mathrm{VEN}}^{\mathrm{SYS}}$	60	$\mathrm{mL/mmHg}$
	$L_{\mathrm{VEN}}^{\mathrm{SYS}}$	5×10^{-4}	$\mathrm{mmHg \cdot s^2/mL}$
	$p_{\mathrm{VEN}}^{\mathrm{SYS}}(0)$	30.9029	mmHg
	$Q_{\mathrm{VEN}}^{\mathrm{SYS}}(0)$	89.6295	mL/s
Pulmonary arteries	$R_{\mathrm{AR}}^{\mathrm{PUL}}$	0.05	$\mathrm{mmHg \cdot s/mL}$
	$C_{\mathrm{AR}}^{\mathrm{PUL}}$	10	$\mathrm{mL/mmHg}$
	$L_{\mathrm{AR}}^{\mathrm{PUL}}$	5×10^{-4}	$\mathrm{mmHg \cdot s^2/mL}$
	$p_{\mathrm{AR}}^{\mathrm{PUL}}(0)$	20.0	mmHg
	$Q_{\mathrm{AR}}^{\mathrm{PUL}}(0)$	69.3166	mL/s
Pulmonary veins	$R_{\mathrm{VEN}}^{\mathrm{PUL}}$	0.025	$\mathrm{mmHg \cdot s/mL}$
	$C_{\mathrm{VEN}}^{\mathrm{PUL}}$	38.4	$\mathrm{mL/mmHg}$
	$L_{\mathrm{VEN}}^{\mathrm{PUL}}$	2.083×10^{-4}	$\mathrm{mmHg \cdot s^2/mL}$
	$p_{\mathrm{VEN}}^{\mathrm{PUL}}(0)$	17.0	mmHg
	$Q_{\mathrm{VEN}}^{\mathrm{PUL}}(0)$	105.523	mL/s

Table 7: Parameters used in the circulation model: systemic and pulmonary circulation.

	Parameter	Value	
Valves	$R_{\min}$	7.5×10^{-3}	$\mathrm{mmHg \cdot s/mL}$
	$R_{\max}$	7.5×10^{4}	$\mathrm{mmHg \cdot s/mL}$
Right atrium	E_{A}	0.06	$\mathrm{mmHg/mL}$
	E_{B}	0.07	$\mathrm{mmHg/mL}$
	t_{C}	0.8	
	T_{C}	0.17	
	T_{R}	0.17	
	$V_{0,\mathrm{RA}}$	4	mL
	$V_{\mathrm{RA}}(0)$	64.1702	mL
Right ventricle	E_{A}	0.55	$\mathrm{mmHg/mL}$
	E_{B}	0.05	$\mathrm{mmHg/mL}$
	t_{C}	0.0	
	T_{C}	0.34	
	T_{R}	0.15	
	$V_{0,\mathrm{RV}}$	16	mL
	$V_{\mathrm{RV}}(0)$	148.9384	mL

Table 8: Parameters used in the circulation model: right heart.

References

[1] P. C. Africa. lifex: a flexible, high performance library for the numerical solution of complex finite element problems. *arXiv preprint arXiv:2207.14668*, 2022.

[2] P. C. Africa, R. Piersanti, M. Fedele, L. Dede', and A. Quarteroni. lifex–heart module: a high-performance simulator for the cardiac function package 1: Fiber generation. *arXiv preprint arXiv:2201.03303*, 2022.

[3] P. C. Africa, M. Salvador, P. Gervasio, L. Dede, and A. Quarteroni. A matrix-free high-order solver for the numerical solution of cardiac electrophysiology. *arXiv preprint arXiv:2205.05136*, 2022.

[4] D. Ambrosi and S. Pezzuto. Active stress vs. active strain in mechanobiology: constitutive issues. *Journal of Elasticity*, 107(2):199–212, 2012.

[5] H. J. Arevalo, F. Vadakkumpadan, E. Guallar, A. Jebb, P. Malamas, K. C. Wu, and N. A. Trayanova. Arrhythmia risk stratification of patients after myocardial infarction using personalized heart models. *Nature Communications*, 7(1):1–8, 2016.

[6] D. Arndt, W. Bangerth, B. Blais, T. C. Clevenger, M. Fehling, A. V. Grayver, T. Heister, L. Heltai, M. Kronbichler, M. Maier, P. Munch, J. Pelteret, R. Rastak, I. Thomas, B. Turcksin, Z. Wang, and D. Wells. The `deal.II` library, version 9.2. *Journal of Numerical Mathematics*, 28(3):131–146, 2020.

[7] D. Arndt, W. Bangerth, D. Davydov, T. Heister, L. Heltai, M. Kronbichler, M. Maier, J. Pelteret, B. Turcksin, and D. Wells. The `deal.II` finite element library: design, features, and insights. *Computers & Mathematics with Applications*, 81:407–422, 2021.

[8] M. Astorino, J.-F. Gerbeau, O. Pantz, and K.-F. Traoré. Fluid–structure interaction and multibody contact: application to aortic valves. *Computer Methods in Applied Mechanics and Engineering*, 198(45-46):3603–3612, 2009.

[9] C. M. Augustin, A. Crozier, A. Neic, A. J. Prassl, E. Karabelas, T. Ferreira da Silva, J. F. Fernandes, F. Campos, T. Kuehne, and G. Plank. Patient-specific modeling of left ventricular electromechanics as a driver for haemodynamic analysis. *EP Europace*, 18:iv121–iv129, 2016.

[10] B. Baillargeon, N. Rebelo, D. D. Fox, R. L. Taylor, and E. Kuhl. The living heart project: a robust and integrative simulator for human heart function. *European Journal of Mechanics-A/Solids*, 48:38–47, 2014.

[11] N. A. Battista and L. A. Miller. Bifurcations in valveless pumping techniques from a coupled fluid-structure-electrophysiology model in heart development. *BIOMATH*, 6(2):ID–1711297, 2017.

[12] J. D. Bayer, R. C. Blake, G. Plank, and N. A. Trayanova. A novel rule-based algorithm for assigning myocardial fiber orientation to computational heart models. *Annals of Biomedical Engineering*, 40(10):2243–2254, 2012.

[13] Y. Bazilevs, V. Calo, J. Cottrell, T. Hughes, A. Reali, and G. Scovazzi. Variational multiscale residual-based turbulence modeling for large eddy simulation of incompressible flows. *Computer Methods in Applied Mechanics and Engineering*, 197(1-4):173–201, 2007.

[14] Y. Bazilevs, K. Takizawa, and T. E. Tezduyar. *Computational fluid-structure interaction: methods and applications*. John Wiley & Sons, 2013.

[15] A. Benchimol and J. G. Ellis. A study of the period of isovolumic relaxation in normal subjects and in patients with heart disease. *The American Journal of Cardiology*, 19(2):196–206, 1967.

[16] E. J. Benjamin, M. J. Blaha, S. E. Chiuve, M. Cushman, S. R. Das, R. Deo, S. D. De Ferranti, J. Floyd, M. Fornage, C. Gillespie, et al. Heart disease and stroke statistics − 2017 update: a report from the american heart association. *Circulation*, 135(10):e146–e603, 2017.

[17] D. Bers. *Excitation-contraction coupling and cardiac contractile force*, volume 237. Springer Science & Business Media, 2001.

[18] C. Bertoglio and A. Caiazzo. A tangential regularization method for backflow stabilization in hemo-dynamics. *Journal of Computational Physics*, 261:162–171, 2014.

[19] P. J. Blanco and R. A. Feijóo. A 3D-1D-0D computational model for the entire cardiovascular system. *Mecánica Computacional*, 29(59):5887–5911, 2010.

[20] D. Bluestein and S. Einav. Transition to turbulence in pulsatile flow through heart valves − a modified stability approach. *Journal of Biomechanical Engineering*, 116(4):477–487, 1994.

[21] J. Brenneisen, A. Daub, T. Gerach, E. Kovacheva, L. Huetter, B. Frohnapfel, O. Dössel, and A. Loewe. Sequential coupling shows minor effects of fluid dynamics on myocardial deformation in a realistic whole-heart model. *Frontiers in Cardiovascular Medicine*, 8(December):1–13, 2021.

[22] M. Bucelli, L. Dede', A. Quarteroni, and C. Vergara. Partitioned and monolithic FSI schemes for the numerical simulation of the heart. *Communications in Computational Physics (to appear)*, 2022.

[23] M. Bucelli, M. G. Gabriel, G. Gigante, L. Dede', A. Quarteroni, and C. Vergara. A stable loosely-coupled scheme for cardiac electro-fluid-structure interaction. *MOX report (to appear), Politecnico di Milano*, 2022.

[24] M. Bucelli, M. Salvador, L. Dede', and A. Quarteroni. Multipatch isogeometric analysis for electro-physiology: simulation in a human heart. *Computer Methods in Applied Mechanics and Engineering*, 376:113666, 2021.

[25] Y. Cheng, H. Oertel, and T. Schenkel. Fluid-structure coupled CFD simulation of the left ventricular flow during filling phase. *Annals of Biomedical Engineering*, 33(5):567–576, 2005.

[26] C. Chnafa, S. Mendez, and F. Nicoud. Image-based large-eddy simulation in a realistic left heart. *Computers & Fluids*, 94:173–187, 2014.

[27] S. Clay, K. Alfakih, A. Radjenovic, T. Jones, and J. P. Ridgway. Normal range of human left ventricular volumes and mass using steady state free precession MRI in the radial long axis orientation. *Magnetic Resonance Materials in Physics, Biology and Medicine*, 19(1):41–45, 2006.

[28] A. Collet. *Numerical modeling of the cardiac mechano-electric feedback within a thermo-electro-mechanical framework. Study of its consequences on arrhythmogenesis*. PhD thesis, Université de Liège, Liège, Belgique, 2015.

[29] P. Colli Franzone, L. F. Pavarino, and S. Scacchi. *Mathematical cardiac electrophysiology*, volume 13. Springer, 2014.

[30] D. Collia, L. Zovatto, and G. Pedrizzetti. Analysis of mitral valve regurgitation by computational fluid dynamics. *APL Bioengineering*, 3(3):036105, 2019.

[31] M. Corti, A. Zingaro, L. Dede, and A. M. Quarteroni. Impact of atrial fibrillation on left atrium haemodynamics: A computational fluid dynamics study. *arXiv preprint arXiv:2202.10893*, 2022.

[32] F. S. Costabal, D. E. Hurtado, and E. Kuhl. Generating Purkinje networks in the human heart. *Journal of Biomechanics*, 49(12):2455–2465, 2016.

[33] Y. Dabiri, J. Yao, K. L. Sack, G. S. Kassab, and J. M. Guccione. Tricuspid valve regurgitation decreases after mitraclip implantation: Fluid structure interaction simulation. *Mechanics Research Communications*, 97:96–100, 2019.

[34] Official deal.ii website. https://www.dealii.org/.

[35] L. Dede', A. Gerbi, and A. Quarteroni. Segregated algorithms for the numerical simulation of cardiac electromechanics in the left human ventricle. In *The mathematics of mechanobiology*, pages 81–116. Springer, 2020.

[36] G. Del Corso, R. Verzicco, and F. Viola. A fast computational model for the electrophysiology of the whole human heart. *Journal of Computational Physics*, 457:111084, 2022.

[37] G. Di Labbio and L. Kadem. Jet collisions and vortex reversal in the human left ventricle. *Journal of Biomechanics*, 78:155–160, 2018.

[38] J. Donea, S. Giuliani, and J.-P. Halleux. An arbitrary Lagrangian-Eulerian finite element method for transient dynamic fluid-structure interactions. *Computer Methods in Applied Mechanics and Engineering*, 33(1-3):689–723, 1982.

[39] R. Doste, D. Soto-Iglesias, G. Bernardino, A. Alcaine, R. Sebastian, S. Giffard-Roisin, M. Sermesant, A. Berruezo, D. Sanchez-Quintana, and O. Camara. A rule-based method to model myocardial fiber orientation in cardiac biventricular geometries with outflow tracts. *International journal for numerical methods in biomedical engineering*, 35(4):e3185, 2019.

[40] M. N. Dusch, S. R. Thadani, G. S. Dhillon, and M. D. Hope. Diastolic function assessed by cardiac MRI using longitudinal left ventricular fractional shortening. *Clinical Imaging*, 38(5):666–668, 2014.

[41] D. R. Einstein, F. Del Pin, X. Jiao, A. P. Kuprat, J. P. Carson, K. S. Kunzelman, R. P. Cochran, J. M. Guccione, and M. B. Ratcliffe. Fluid–structure interactions of the mitral valve and left heart: comprehensive strategies, past, present and future. *International Journal for Numerical Methods in Biomedical Engineering*, 26(3-4):348–380, 2010.

[42] K. Emilsson, R. Egerlid, B.-M. Nygren, and B. Wandt. Mitral annulus motion versus long-axis fractional shortening. *Experimental & Clinical Cardiology*, 11(4):302, 2006.

[43] T. S. Eriksson, A. J. Prassl, G. Plank, and G. A. Holzapfel. Influence of myocardial fiber/sheet orientations on left ventricular mechanical contraction. *Mathematics and Mechanics of Solids*, 18(6):592–606, 2013.

[44] J. Fabian, E. Epstein, and N. Coulshed. Duration of phases of left ventricular systole using indirect methods. I. normal subjects. *British Heart Journal*, 34(9):874, 1972.

[45] M. Fedele, E. Faggiano, L. Dede', and A. Quarteroni. A patient-specific aortic valve model based on moving resistive immersed implicit surfaces. *Biomechanics and Modeling in Mechanobiology*, 16(5):1779–1803, 2017.

[46] M. Fedele, R. Piersanti, F. Regazzoni, M. Salvador, P. C. Africa, M. Bucelli, A. Zingaro, L. Dede', and A. Quarteroni. A comprehensive and biophysically detailed computational model of the whole human heart electromechanics. *arXiv preprint arXiv:2207.12460*, 2022.

[47] M. Fedele and A. Quarteroni. Polygonal surface processing and mesh generation tools for the numerical simulation of the cardiac function. *International Journal for Numerical Methods in Biomedical Engineering*, 37(4):e3435, 2021.

[48] J. J. Feher. *Quantitative human physiology: an introduction*. Academic press, 2017.

[49] L. Feng, H. Gao, B. Griffith, S. Niederer, and X. Luo. Analysis of a coupled fluid-structure interaction model of the left atrium and mitral valve. *International Journal for Numerical Methods in Biomedical Engineering*, 35(11):e3254, 2019.

[50] I. Fumagalli. A reduced 3D-0D FSI model of the aortic valve including leaflets curvature. *arXiv preprint arXiv:2106.00571*, 2021.

[51] I. Fumagalli, M. Fedele, C. Vergara, L. Dede', S. Ippolito, F. Nicolò, C. Antona, R. Scrofani, and A. Quarteroni. An image-based computational hemodynamics study of the systolic anterior motion of the mitral valve. *Computers in Biology and Medicine*, 123:103922, 2020.

[52] I. Fumagalli, P. Vitullo, C. Vergara, M. Fedele, A. F. Corno, S. Ippolito, R. Scrofani, and A. Quarteroni. Image-based computational hemodynamics analysis of systolic obstruction in hypertrophic cardiomyopathy. *Frontiers in Physiology*, page 2437, 2022.

[53] H. Gao, L. Feng, N. Qi, C. Berry, B. E. Griffith, and X. Luo. A coupled mitral valve–left ventricle model with fluid–structure interaction. *Medical Engineering & Physics*, 47:128–136, 2017.

[54] T. Gerach, S. Schuler, J. Fröhlich, L. Lindner, E. Kovacheva, R. Moss, E. M. Wülfers, G. Seemann, C. Wieners, and A. Loewe. Electro-mechanical whole-heart digital twins: a fully coupled multi-physics approach. *Mathematics*, 9(11):1247, 2021.

[55] A. Gerbi. *Numerical approximation of cardiac electro-fluid-mechanical models*. PhD thesis, EPFL, 2018.

[56] A. Gerbi, L. Dede', and A. Quarteroni. A monolithic algorithm for the simulation of cardiac electromechanics in the human left ventricle. *Mathematics in Engineering*, 1(1):1–37, 2019.

[57] D. Gil, R. Aris, A. Borras, E. Ramírez, R. Sebastian, and M. Vazquez. Influence of fiber connectivity in simulations of cardiac biomechanics. *International Journal of Computer Assisted Radiology and Surgery*, 14(1):63–72, 2019.

[58] K. Gillette, M. A. Gsell, A. J. Prassl, E. Karabelas, U. Reiter, G. Reiter, T. Grandits, C. Payer, D. Štern, M. Urschler, J. D. Bayer, C. M. Augustin, A. Neic, T. Pock, E. J. Vigmond, and G. Plank. A framework for the generation of digital twins of cardiac electrophysiology from clinical 12-leads ECGs. *Medical Image Analysis*, 71:102080, 2021.

[59] S. Göktepe and E. Kuhl. Electromechanics of the heart: a unified approach to the strongly coupled excitation–contraction problem. *Computational Mechanics*, 45(2):227–243, 2010.

[60] R. A. Gray and P. Pathmanathan. Patient-specific cardiovascular computational modeling: diversity of personalization and challenges. *Journal of Cardiovascular Translational Research*, 11(2):80–88, 2018.

[61] J. M. Guccione and A. D. McCulloch. Finite element modeling of ventricular mechanics. In *Theory of Heart*, pages 121–144. Springer, 1991.

[62] G. Gulsin, A. Singh, and G. P. McCann. Cardiovascular magnetic resonance in the evaluation of heart valve disease. *BMC Medical Imaging*, 17(1):1–14, 2017.

[63] V. Gurev, T. Lee, J. Constantino, H. Arevalo, and N. A. Trayanova. Models of cardiac electromechanics based on individual hearts imaging data: Image-based electromechanical models of the heart. *Biomechanics and Modeling in Mechanobiology*, 10(3):295–306, 2011.

[64] K. Hammermeister, R. Brooks, and J. Warbasse. The rate of change of left ventricular volume in man: I. validation and peak systolic ejection rate in health and disease. *Circulation*, 49(4):729–738, 1974.

[65] E. W. Hawthorne. Dynamic geometry of the left ventricle. *The American Journal of Cardiology*, 18(4):566–573, 1966.

[66] M. Hirschhorn, V. Tchantchaleishvili, R. Stevens, J. Rossano, and A. Throckmorton. Fluid–structure interaction modeling in cardiovascular medicine – a systematic review 2017–2019. *Medical Engineering & Physics*, 78:1–13, 2020.

[67] M. Hirschvogel, M. Bassilious, L. Jagschies, S. M. Wildhirt, and M. W. Gee. A monolithic 3D-0D coupled closed-loop model of the heart and the vascular system: experiment-based parameter estimation for patient-specific cardiac mechanics. *International Journal for Numerical Methods in Biomedical Engineering*, 33(8):e2842, 2017.

[68] J. Hoffman, J. Jansson, and M. Stöckli. Unified continuum modeling of fluid-structure interaction. *Mathematical Models and Methods in Applied Sciences*, 21(03):491–513, 2011.

[69] A. Hosoi, T. Washio, J.-i. Okada, Y. Kadooka, K. Nakajima, and T. Hisada. A multi-scale heart simulation on massively parallel computers. In *SC'10: Proceedings of the 2010 ACM/IEEE International Conference for High Performance Computing, Networking, Storage and Analysis*, pages 1–11. IEEE, 2010.

[70] M.-C. Hsu, D. Kamensky, Y. Bazilevs, M. S. Sacks, and T. J. Hughes. Fluid–structure interaction analysis of bioprosthetic heart valves: significance of arterial wall deformation. *Computational Mechanics*, 54(4):1055–1071, 2014.

[71] T. J. Hughes. *The finite element method: linear static and dynamic finite element analysis*. Courier Corporation, 2012.

[72] T. J. R. Hughes, W. K. Liu, and T. K. Zimmermann. Lagrangian-eulerian finite element formulation for incompressible viscous flows. *Computer Methods in Applied Mechanics and Engineering*, 29(3):329–349, 1981.

[73] R. Jacob, B. Dierberger, and G. Kissling. Functional significance of the frank-starling mechanism under physiological and pathophysiological conditions. *European heart journal*, 13(suppl_E):7–14, 1992.

[74] J. Janela, A. B. de Moura, and A. Sequeira. Comparing absorbing boundary conditions for a 3d non newtonian fluid-structure interaction model for blood flow in arteries. *Mecánica Computacional*, 29(59):5961–5971, 2010.

[75] C.-S. Jhun, R. Newswanger, J. P. Cysyk, S. Ponnaluri, B. Good, K. B. Manning, and G. Rosenberg. Dynamics of blood flows in aortic stenosis: mild, moderate, and severe. *ASAIO Journal*, 67(6):666–674, 2021.

[76] A. A. Johnson and T. E. Tezduyar. Mesh update strategies in parallel finite element computations of flow problems with moving boundaries and interfaces. *Computer Methods in Applied Mechanics and Engineering*, 119(1-2):73–94, 1994.

[77] E. Karabelas, S. Longobardi, J. Fuchsberger, O. Razeghi, C. Rodero, M. Strocchi, R. Rajani, G. Haase, G. Plank, and S. Niederer. Global sensitivity analysis of four chamber heart hemodynamics using surrogate models. *IEEE Transactions on Biomedical Engineering*, 2022.

[78] T. Kariya, T. Washio, J.-i. Okada, M. Nakagawa, M. Watanabe, Y. Kadooka, S. Sano, R. Nagai, S. Sugiura, and T. Hisada. Personalized perioperative multi-scale, multi-physics heart simulation of double outlet right ventricle. *Annals of Biomedical Engineering*, 48(6):1740–1750, 2020.

[79] A. M. Katz. *Physiology of the Heart*. Lippincott Williams & Wilkins, 2010.

[80] S. Khodaei, A. Henstock, R. Sadeghi, S. Sellers, P. Blanke, J. Leipsic, A. Emadi, and Z. Keshavarz-Motamed. Personalized intervention cardiology with transcatheter aortic valve replacement made possible with a non-invasive monitoring and diagnostic framework. *Scientific Reports*, 11(1):1–28, 2021.

[81] R. Klabunde. *Cardiovascular physiology concepts*. Lippincott Williams & Wilkins, 2011.

[82] S. Krishnamoorthi, M. Sarkar, and W. S. Klug. Numerical quadrature and operator splitting in finite element methods for cardiac electrophysiology. *International Journal for Numerical Methods in Biomedical Engineering*, 29(11):1243–1266, 2013.

[83] J. Kronborg, F. Svelander, S. Eriksson-Lidbrink, L. Lindström, C. Homs-Pons, D. Lucor, and J. Hoffman. Computational analysis of flow structures in turbulent ventricular blood flow associated with mitral valve intervention. *Frontiers in Physiology*, page 752, 2022.

[84] V. Kumar, A. K. Abbas, N. Fausto, and J. C. Aster. *Robbins and Cotran pathologic basis of disease, professional edition e-book*. Elsevier health sciences, 2014.

[85] M. Landajuela, C. Vergara, A. Gerbi, L. Dedè, L. Formaggia, and A. Quarteroni. Numerical approximation of the electromechanical coupling in the left ventricle with inclusion of the Purkinje network. *International Journal for Numerical Methods in Biomedical Engineering*, 34(7):e2984, 2018.

[86] F. Levrero-Florencio, F. Margara, E. Zacur, A. Bueno-Orovio, Z. Wang, A. Santiago, J. Aguado-Sierra, G. Houzeaux, V. Grau, D. Kay, M. Vázquez, R. Ruiz-Baier, and B. Rodriguez. Sensitivity analysis of a strongly-coupled human-based electromechanical cardiac model: Effect of mechanical parameters on physiologically relevant biomarkers. *Computer Methods in Applied Mechanics and Engineering*, 361:112762, 2020.

[87] Official life^x website. https://lifex.gitlab.io/.

[88] W. C. Little and T. R. Downes. Clinical evaluation of left ventricular diastolic performance. *Progress in Cardiovascular Diseases*, 32(4):273–290, 1990.

[89] G. Luraghi, W. Wu, F. De Gaetano, J. F. R. Matas, G. D. Moggridge, M. Serrani, J. Stasiak, M. L. Costantino, and F. Migliavacca. Evaluation of an aortic valve prosthesis: Fluid-structure interaction or structural simulation? *Journal of Biomechanics*, 58:45–51, 2017.

[90] X. Ma, H. Gao, B. E. Griffith, C. Berry, and X. Luo. Image-based fluid–structure interaction model of the human mitral valve. *Computers & Fluids*, 71:417–425, 2013.

[91] A. M. Maceira, S. K. Prasad, M. Khan, and D. J. Pennell. Normalized left ventricular systolic and diastolic function by steady state free precession cardiovascular magnetic resonance. *Journal of Cardiovascular Magnetic Resonance*, 8(3):417–426, 2006.

[92] J. B. Mark. *Atlas of cardiovascular monitoring*. Churchill Livingstone, 1998.

[93] M. E. Moghadam, Y. Bazilevs, T.-Y. Hsia, I. E. Vignon-Clementel, and A. L. Marsden. A comparison of outlet boundary treatments for prevention of backflow divergence with relevance to blood flow simulations. *Computational Mechanics*, 48(3):277–291, 2011.

[94] J. P. Murgo, N. Westerhof, J. P. Giolma, and S. A. Altobelli. Aortic input impedance in normal man: relationship to pressure wave forms. *Circulation*, 62(1):105–116, 1980.

[95] M. P. Nash and A. V. Panfilov. Electromechanical model of excitable tissue to study reentrant cardiac arrhythmias. *Progress in biophysics and molecular biology*, 85(2-3):501–522, 2004.

[96] S. A. Niederer, J. Lumens, and N. A. Trayanova. Computational models in cardiology. *Nature Reviews Cardiology*, 16(2):100–111, 2019.

[97] D. Nordsletten, M. McCormick, P. Kilner, P. Hunter, D. Kay, and N. Smith. Fluid–solid coupling for the investigation of diastolic and systolic human left ventricular function. *International Journal for Numerical Methods in Biomedical Engineering*, 27(7):1017–1039, 2011.

[98] R. Ogden. *Non-Linear Elastic Deformations*. Courier Corporation, 2013.

[99] J.-i. Okada, T. Washio, S. Sugiura, and T. Hisada. Clinical and pharmacological application of multiscale multiphysics heart simulator, UT-Heart. *The Korean Journal of Physiology & Pharmacology*, 23(5):295–303, 2019.

[100] L. H. Opie. *Heart physiology: from cell to circulation*. Lippincott Williams & Wilkins, 2004.

[101] N. G. Pandian, D. J. Skorton, S. M. Collins, H. L. Falsetti, E. R. Burke, and R. E. Kerber. Heterogeneity of left ventricular segmental wall thickening and excursion in 2-dimensional echocardiograms of normal human subjects. *The American journal of cardiology*, 51(10):1667–1673, 1983.

[102] P. Pathmanathan, S. Chapman, D. Gavaghan, and J. Whiteley. Cardiac electromechanics: the effect of contraction model on the mathematical problem and accuracy of the numerical scheme. *The Quarterly Journal of Mechanics & Applied Mathematics*, 63(3):375–399, 2010.

[103] P. Pathmanathan, G. R. Mirams, J. Southern, and J. P. Whiteley. The significant effect of the choice of ionic current integration method in cardiac electro-physiological simulations. *International Journal for Numerical Methods in Biomedical Engineering*, 27(11):1751–1770, 2011.

[104] G. Pedrizzetti, G. La Canna, O. Alfieri, and G. Tonti. The vortex – an early predictor of cardiovascular outcome? *Nature Reviews Cardiology*, 11(9):545–553, 2014.

[105] M. R. Pfaller, J. M. Hörmann, M. Weigl, A. Nagler, R. Chabiniok, C. Bertoglio, and W. A. Wall. The importance of the pericardium for cardiac biomechanics: from physiology to computational modeling. *Biomechanics and Modeling in Mechanobiology*, 18(2):503–529, 2019.

[106] R. Piersanti, P. C. Africa, M. Fedele, C. Vergara, L. Dede', A. F. Corno, and A. Quarteroni. Modeling cardiac muscle fibers in ventricular and atrial electrophysiology simulations. *Computer Methods in Applied Mechanics and Engineering*, 373:113468, 2021.

[107] R. Piersanti, F. Regazzoni, M. Salvador, A. F. Corno, C. Vergara, A. Quarteroni, et al. 3D–0D closed-loop model for the simulation of cardiac biventricular electromechanics. *Computer Methods in Applied Mechanics and Engineering*, 391:114607, 2022.

[108] A. Quarteroni. *Numerical Models for Differential Problems*, volume 16. Springer, 2017.

[109] A. Quarteroni, L. Dede', A. Manzoni, and C. Vergara. *Mathematical modelling of the human cardiovascular system: data, numerical approximation, clinical applications*, volume 33. Cambridge University Press, 2019.

[110] A. Quarteroni, T. Lassila, S. Rossi, and R. Ruiz-Baier. Integrated heart – coupling multiscale and multiphysics models for the simulation of the cardiac function. *Computer Methods in Applied Mechanics and Engineering*, 314:345–407, 2017.

[111] A. Quarteroni, A. Veneziani, and C. Vergara. Geometric multiscale modeling of the cardiovascular system, between theory and practice. *Computer Methods in Applied Mechanics and Engineering*, 302:193–252, 2016.

[112] F. Regazzoni. *Mathematical modeling and Machine Learning for the numerical simulation of cardiac electromechanics*. PhD thesis, Politecnico di Milano, 2020.

[113] F. Regazzoni, L. Dede', and A. Quarteroni. Biophysically detailed mathematical models of multiscale cardiac active mechanics. *PLoS Computational Biology*, 16(10):e1008294, 2020.

[114] F. Regazzoni and A. Quarteroni. An oscillation-free fully staggered algorithm for velocity-dependent active models of cardiac mechanics. *Computer Methods in Applied Mechanics and Engineering*, 373:113506, 2021.

[115] F. Regazzoni, M. Salvador, P. C. Africa, M. Fedele, L. Dede', and A. Quarteroni. A cardiac electrome-chanical model coupled with a lumped-parameter model for closed-loop blood circulation. *Journal of Computational Physics*, 457:111083, 2022.

[116] G. Rigatelli, C. Chiastra, G. Pennati, G. Dubini, F. Migliavacca, and M. Zuin. Applications of compu-tational fluid dynamics to congenital heart diseases: a practical review for cardiovascular professionals. *Expert Review of Cardiovascular Therapy*, 19(10):907–916, 2021.

[117] D. E. Roberts, L. T. Hersh, and A. M. Scher. Influence of cardiac fiber orientation on wavefront voltage, conduction velocity, and tissue resistivity in the dog. *Circulation Research*, 44(5):701–712, 1979.

[118] D. Romero, R. Sebastian, B. H. Bijnens, V. Zimmerman, P. M. Boyle, E. J. Vigmond, and A. F. Frangi. Effects of the Purkinje system and cardiac geometry on biventricular pacing: a model study. *Annals of Biomedical Engineering*, 38(4):1388–1398, 2010.

[119] S. Rossi, T. Lassila, R. Ruiz-Baier, A. Sequeira, and A. Quarteroni. Thermodynamically consistent orthotropic activation model capturing ventricular systolic wall thickening in cardiac electromechanics. *European Journal of Mechanics-A/Solids*, 48:129–142, 2014.

[120] Y. Saad. *Iterative methods for sparse linear systems*. SIAM, 2003.

[121] Y. Sahasakul, W. D. Edwards, J. M. Naessens, and A. J. Tajik. Age-related changes in aortic and mitral valve thickness: implications for two-dimensional echocardiography based on an autopsy study of 200 normal human hearts. *The American journal of cardiology*, 62(7):424–430, 1988.

[122] M. Salvador, L. Dede', and A. Quarteroni. An intergrid transfer operator using radial basis functions with application to cardiac electromechanics. *Computational Mechanics*, 66:491–511, 2020.

[123] M. Salvador, M. Fedele, P. C. Africa, E. Sung, L. Dede', A. Prakosa, J. Chrispin, N. Trayanova, and A. Quarteroni. Electromechanical modeling of human ventricles with ischemic cardiomyopathy: numerical simulations in sinus rhythm and under arrhythmia. *Computers in Biology and Medicine*, 136:104674, 2021.

[124] M. Salvador, F. Regazzoni, S. Pagani, N. Trayanova, A. Quarteroni, et al. The role of mechano-electric feedbacks and hemodynamic coupling in scar-related ventricular tachycardia. *Computers in Biology and Medicine*, 142:105203, 2022.

[125] A. Santiago, J. Aguado-Sierra, M. Zavala-Aké, R. Doste-Beltran, S. Gómez, R. Arís, J. C. Cajas, E. Casoni, and M. Vázquez. Fully coupled fluid-electro-mechanical model of the human heart for su-percomputers. *International Journal for Numerical Methods in Biomedical Engineering*, 34(12):e3140, 2018.

[126] N. Smith, D. Nickerson, E. Crampin, and P. Hunter. Multiscale computational modelling of the heart. *Acta Numerica*, 13:371–431, 2004.

[127] J. H. Spühler and J. Hoffman. An interface-tracking unified continuum model for fluid-structure inter-action with topology change and full-friction contact with application to aortic valves. *International Journal for Numerical Methods in Engineering*, 122(19):5258–5278, 2021.

[128] J. H. Spühler, J. Jansson, N. Jansson, and J. Hoffman. 3D fluid-structure interaction simulation of aortic valves using a unified continuum ALE FEM model. *Frontiers in Physiology*, 9:363, 2018.

[129] J. H. Spühler, J. Jansson, N. Jansson, and J. Hoffman. A high performance computing framework for finite element simulation of blood flow in the left ventricle of the human heart. In *Numerical methods for flows*, pages 155–164. Springer, 2020.

[130] C. L. Stanfield. *Principles of human physiology*. Pearson, 2016.

[131] K. Stein, T. Tezduyar, and R. Benney. Mesh moving techniques for fluid-structure interactions with large displacements. *Journal of Applied Mechanics*, 70(1):58–63, 2003.

[132] M. Strocchi, M. A. Gsell, C. M. Augustin, O. Razeghi, C. H. Roney, A. J. Prassl, E. J. Vigmond, J. M. Behar, J. S. Gould, C. A. Rinaldi, M. J. Bishop, G. Plank, and S. A. Niederer. Simulating ventricular systolic motion in a four-chamber heart model with spatially varying Robin boundary conditions to model the effect of the pericardium. *Journal of Biomechanics*, 101:109645, 2020.

[133] T. Sugimoto, R. Dulgheru, A. Bernard, F. Ilardi, L. Contu, K. Addetia, L. Caballero, N. Akhaladze, G. D. Athanassopoulos, D. Barone, et al. Echocardiographic reference ranges for normal left ventricular 2D strain: results from the EACVI NORRE study. *European Heart Journal-Cardiovascular Imaging*, 18(8):833–840, 2017.

[134] S. Sugiura, J.-I. Okada, T. Washio, and T. Hisada. Ut-heart: A finite element model designed for the multiscale and multiphysics integration of our knowledge on the human heart. In *Computational Systems Biology in Medicine and Biotechnology*, pages 221–245. Springer, 2022.

[135] J. Sundnes, G. T. Lines, X. Cai, B. F. Nielsen, K.-A. Mardal, and A. Tveito. *Computing the electrical activity in the heart*, volume 1. Springer Science & Business Media, 2007.

[136] K. H. Ten Tusscher and A. V. Panfilov. Alternans and spiral breakup in a human ventricular tissue model. *American Journal of Physiology-Heart and Circulatory Physiology*, 291(3):H1088–H1100, 2006.

[137] T. Terahara, T. Kuraishi, K. Takizawa, and T. E. Tezduyar. Computational flow analysis with boundary layer and contact representation: II. heart valve flow with leaflet contact. *Journal of Mechanics*, 38:185–194, 2022.

[138] T. Terahara, K. Takizawa, T. E. Tezduyar, Y. Bazilevs, and M.-C. Hsu. Heart valve isogeometric sequentially-coupled FSI analysis with the space–time topology change method. *Computational Mechanics*, 65:1167–1187, 2020.

[139] A. This, L. Boilevin-Kayl, M. A. Fernández, and J.-F. Gerbeau. Augmented resistive immersed surfaces valve model for the simulation of cardiac hemodynamics with isovolumetric phases. *International Journal for Numerical Methods in Biomedical Engineering*, 36(3):e3223, 2020.

[140] N. A. Trayanova. Whole-heart modeling: applications to cardiac electrophysiology and electromechanics. *Circulation Research*, 108(1):113–128, 2011.

[141] T. P. Usyk, I. J. LeGrice, and A. D. McCulloch. Computational model of three-dimensional cardiac electromechanics. *Computing and Visualization in Science*, 4(4):249–257, 2002.

[142] V. Vedula, J.-H. Seo, A. C. Lardo, and R. Mittal. Effect of trabeculae and papillary muscles on the hemodynamics of the left ventricle. *Theoretical and Computational Fluid Dynamics*, 30(1):3–21, 2016.

[143] C. Vergara, M. Lange, S. Palamara, T. Lassila, A. F. Frangi, and A. Quarteroni. A coupled 3D–1D numerical monodomain solver for cardiac electrical activation in the myocardium with detailed Purkinje network. *Journal of Computational Physics*, 308:218–238, 2016.

[144] A. Verkaik, A. Bogaerds, F. Storti, and F. Van De Vosse. A coupled overlapping domain method for the computation of transitional flow through artificial heart valves. In *ASME 2012 Summer Bioengineering Conference (SBC 2012)*, pages 217–218. American Society of Mechanical Engineers, 2012.

[145] R. Verzicco. Electro-fluid-mechanics of the heart. *Journal of Fluid Mechanics*, 941, 2022.

[146] I. E. Vignon-Clementel, C. Figueroa, K. Jansen, and C. Taylor. Outflow boundary conditions for 3D simulations of non-periodic blood flow and pressure fields in deformable arteries. *Computer Methods in Biomechanics and Biomedical Engineering*, 13(5):625–640, 2010.

[147] F. Viola, V. Meschini, and R. Verzicco. Fluid–structure–electrophysiology interaction (FSEI) in the left-heart: a multi-way coupled computational model. *European Journal of Mechanics-B/Fluids*, 79:212–232, 2020.

[148] F. Viola, V. Meschini, and R. Verzicco. Effects of stenotic aortic valve on the left heart hemodynamics: A fluid-structure-electrophysiology approach. *arXiv preprint arXiv:2103.14680*, 2021.

[149] F. Viola, V. Spandan, V. Meschini, J. Romero, M. Fatica, M. D. de Tullio, and R. Verzicco. FSEI-GPU: GPU accelerated simulations of the fluid–structure–electrophysiology interaction in the left heart. *Computer Physics Communications*, 273:108248, 2022.

[150] VMTK. Website: http://www.vmtk.org/; code repository: https://github.com/marco-fedele/vmtk.

[151] P. Wood. Aortic stenosis. *The American Journal of Cardiology*, 1(5):553–571, 1958.

[152] J. Xu and L. Zikatanov. Algebraic multigrid methods. *Acta Numerica*, 26:591–721, 2017.

[153] Q. Zhang and T. Hisada. Analysis of fluid–structure interaction problems with structural buckling and large domain changes by ALE finite element method. *Computer Methods in Applied Mechanics and Engineering*, 190(48):6341–6357, 2001.

[154] A. Zingaro, M. Bucelli, I. Fumagalli, L. Dede', and A. Quarteroni. Modeling isovolumetric phases in cardiac flows by an Augmented Resistive Immersed Implicit Surface method. *MOX report (to appear), Politecnico di Milano*, 2022.

[155] A. Zingaro, L. Dede', F. Menghini, and A. Quarteroni. Hemodynamics of the heart's left atrium based on a variational multiscale-LES numerical method. *European Journal of Mechanics-B/Fluids*, 89:380–400, 2021.

[156] A. Zingaro, I. Fumagalli, L. Dede', M. Fedele, P. C. Africa, A. F. Corno, and A. Quarteroni. A geometric multiscale model for the numerical simulation of blood flow in the human left heart. *Discrete & Continuous Dynamical Systems-S*, 15(8):2391–2427, 2022.

[157] Zygote Media Group Inc. Zygote solid 3D heart generation II developement report. Technical report. 2014.

MOX Technical Reports, last issues

Dipartimento di Matematica
Politecnico di Milano, Via Bonardi 9 - 20133 Milano (Italy)

51/2022   Losapio, D.; Scotti, A.
Local Embedded Discrete Fracture Model (LEDFM)

52/2022   Fedele, M.; Piersanti, R.; Regazzoni, F.; Salvador, M.; Africa, P. C.; Bucelli, M.; Zingaro, A.; I
A comprehensive and biophysically detailed computational model of the whole human heart electromechanics

50/2022   Elías, A.; Jiménez, R.; Paganoni, A.M.; Sangalli, L.M.
Integrated Depths for Partially Observed Functional Data

53/2022   Antonietti, P.F; Cauzzi, C.; Mazzieri, I.; Melas L.; Stupazzini, M.
Numerical simulation of the Athens 1999 earthquake including simplified models of the Acropolis and the Parthenon: initial results and outlook

47/2022   Botti, M.; Di Pietro, D.A.; Salah, M.
A serendipity fully discrete div-div complex on polygonal meshes

49/2022   Botti, M.; Fumagalli, A.; Scotti, A.
Uncertainty quantification for mineral precipitation and dissolution in fractured porous media

48/2022   Gregorio, C.; Barbati, G.; Ieva, F.
A wavelet-mixed landmark survival model for the effect of short-term oscillations in longitudinal biomarker's profiles

45/2022   Franco, N.; Fresca, S.; Manzoni, A.; Zunino, P.
Approximation bounds for convolutional neural networks in operator learning

46/2022   Lucca, A.; Fraccarollo, L.; Fossan, F.E.; Braten, A.T.; Pozzi, S.; Vergara, C.; Muller, L.O.
Impact of pressure guidewire on model-based FFR prediction

44/2022   Peli, R.; Dovera, L.; Fighera, G.; Menafoglio, A.; Secchi, P.
Forecasting Oil Production Rates in Primary Depletion using the Physics-based Residual Kriging functional approach